Sources of Drag in Estuarine Meanders: Momentum Redistribution, Bottom Stress Enhancement, and Bend-Scale Form Drag

TONG BO,[a,b] DAVID K. RALSTON,[a] AND W. ROCKWELL GEYER[a]

[a] *Applied Ocean Physics and Engineering Department, Woods Hole Oceanographic Institution, Woods Hole, Massachusetts*
[b] *MIT-WHOI Joint Program in Oceanography/Applied Ocean Science and Engineering, Cambridge and Woods Hole, Massachusetts*

(Manuscript received 19 October 2022, in final form 3 February 2023, accepted 29 March 2023)

ABSTRACT: Curvature can create secondary circulation and flow separation in tidal channels, and both have important consequences for the along-channel momentum budget. The North River is a sinuous estuary where drag is observed to be higher than expected, and a numerical model is used to investigate the influence of curvature-induced processes on the momentum distribution and drag. The hydrodynamic drag is greatly increased in channel bends compared to that for straight channel flows. Drag coefficients are calculated using several approaches to identify the different factors contributing to the drag increase. Flow separation creates low-pressure recirculation zones on the lee side of the bends and results in form drag. Form drag is the dominant source of the increase in total drag during flood tides and is less of a factor during ebb tides. During both floods and ebbs, curvature-induced secondary circulation transports higher-momentum fluid to the lower water column through vertical and lateral advection. Consequently, the streamwise velocity profile deviates from the classic log profile and vertical shear becomes more concentrated near the bed. This redistribution by the lateral circulation causes an overall increase in bottom friction and contributes to the increased drag. Additionally, spatial variations in the depth-averaged velocity field due to the curvature-induced flow are nonlinearly correlated with the bathymetric structure, leading to increased bottom friction. In addition to affecting the tidal flow, the redistributed momentum and altered bottom shear stress have clear implications for channel morphodynamics.

KEYWORDS: Estuaries; Channel flows; Secondary circulation; Boundary layer; Tides; Numerical analysis/modeling

1. Introduction

Meanders are ubiquitously found in rivers and tidal channels (e.g., Langbein and Leopold 1970; Marani et al. 2002; Fagherazzi et al. 2004). Distinct flow processes can occur in channel bends as a result of the curvature effect, including secondary circulation (e.g., Thomson 1877; Kalkwijk and Booij 1986) and flow separation (e.g., Leopold 1960; Leeder and Bridges 1975). These curvature-induced hydrodynamic processes can significantly alter the streamwise momentum distribution in channel bends and therefore affect the along-channel momentum balance (e.g., Leopold 1960; Chang 1984; Seim et al. 2002; Blanckaert and Graf 2004).

The drag force is a dominant sink term in the momentum budget that opposes the streamwise flow. The drag coefficient C_d is one of the typical ways to quantify the momentum loss, here defined as

$$C_d = \frac{\tau_t}{\rho \overline{u}|\overline{u}|}, \tag{1}$$

where τ_t is the total drag, ρ is density, and $\overline{u}$ is the depth-averaged velocity. In shallow flows (e.g., in estuaries, rivers, and the coastal ocean), drag is mainly attributed to the bottom shear stress τ_b, i.e., $\tau_t = \tau_b$. Shallow flows typically have a logarithmic velocity in the bottom boundary layer, also known as the log law (e.g., Monin and Yaglom 1971; Trowbridge and Lentz 2018),

$$u = \frac{u_*}{\kappa} \ln\left(\frac{z}{z_0}\right), \tag{2}$$

where u is the streamwise velocity,

$$u_* = \sqrt{\frac{\tau_b}{\rho}} \tag{3}$$

is the shear velocity, $\kappa \approx 0.41$ is the Von Kármán constant, z is the distance above the channel bed, and z_0 is the bottom roughness length scale. Therefore, a dependence of C_d on H and z_0 can be obtained by combining (1)–(3) (e.g., Gross et al. 1999; Bricker et al. 2005; Lentz et al. 2017),

$$C_d = \left[\frac{\kappa}{\ln\left(\frac{H}{z_0}\right) - 1}\right]^2, \tag{4}$$

with H being the water depth. In addition, a Coles' wake function may be added to (2) and (4) to account for deviations from the log law (Coles 1956; Lentz et al. 2017). Common values for C_d used in estuaries and tidal channels are around 0.003–0.004 (e.g., Soulsby 1990; Geyer et al. 2000), e.g., for $H = 5$ m and $z_0 = 0.002$–0.005 m.

The overall drag force directly affects the large-scale estuarine momentum balance, with consequences for tidal propagation, flooding potential, and marsh inundation. On the other hand, the local drag from bottom shear stress reflects the intensity of turbulence, which determines the strength of

Supplemental information related to this paper is available at the Journals Online website: https://doi.org/10.1175/JPO-D-22-0211.s1.

Corresponding author: Tong Bo, tongbo@mit.edu

DOI: 10.1175/JPO-D-22-0211.1

local mixing processes and rate of bed sediment erosion or deposition. Various factors can alter the flow structure, affect the momentum balance and drag, and lead to deviations of C_d from the typical value, including bedforms (Fong et al. 2009), vegetation (Nepf 1999), stratification (Friedrichs and Wright 1997), and large topographic features such as headlands (McCabe et al. 2006) and meanders (Seim et al. 2006).

Channel meanders can affect the momentum distribution and drag in an estuary through both secondary circulation and flow separation. The curvature-induced secondary circulation typically results from the local imbalance between the lateral pressure gradient and centrifugal acceleration. Open-channel flow with curvature generates a water-level setup near the outer bank and a setdown near the inner bank, and the resulting inward pressure gradient forcing balances the outward centrifugal acceleration in the lateral direction (Thomson 1877; Kalkwijk and Booij 1986). The above two forcing terms have a depth-dependent imbalance because the along-channel flow is vertically sheared, and therefore, secondary circulation develops in the lateral plane, typically with inward flow near the bottom and outward flow near the surface, and with downwelling near the outer bank and upwelling near the inner bank for mass conservation. In estuaries, salinity variations can cause internal deformations in the density field and create lateral pressure gradients in addition to those due to water-level disturbances, which thus affect the secondary circulation in bends (e.g., Lacy and Monismith 2001; Nidzieko et al. 2009; Kranenburg et al. 2019).

Secondary circulation has been found to influence the streamwise momentum distribution and hydrodynamic drag in both laboratory and natural meanders (e.g., Chow 1959; Chang 1983; Seim et al. 2002; Blanckaert and Graf 2004). Laboratory experiments have demonstrated that secondary circulation can increase the drag by creating an additional lateral bed shear stress component (e.g., Chang 1983, 1984; Blanckaert and de Vriend 2003). Furthermore, bottom stress can be enhanced as a result of the vertical advection of streamwise momentum (Einstein and Harder 1954; Blanckaert and Graf 2004; Blanckaert and De Vriend 2010). A Manning's n is an engineering coefficient typically used to quantify the effect of friction for open channel flows, and meanders were found to have Manning's n values up to 30% greater than straight channels in the laboratory (Chow 1959). In natural rivers meanders, Arcement and Schneider (1989) also suggested increased values of Manning's n to account for the increased drag. In a curved estuarine channel in San Francisco Bay, secondary circulation was found to laterally transport the high momentum from the center of the channel toward the sides (Lacy and Monismith 2001), but the influence of the redistributed momentum on the bed shear stress was not investigated. Seim et al. (2002) observed high bottom shear stress in the sinuous Satilla River estuary and attributed it to the vertical advection of high velocity to the bed by secondary circulation, but the measurements did not fully resolve the flow field.

In addition to generating secondary circulation, curvature can induce horizontal flow separation in bends (Leeder and Bridges 1975; Leopold 1960). The water-level setdown near the inner bank relaxes downstream of the bend apex as the curvature effect decreases, and this creates an adverse pressure gradient along the inner bank (Blanckaert 2010; Vermeulen et al. 2015; Bo and Ralston 2020). The adverse pressure gradient decreases the velocity near the inner bank and, as a result, can cause the main flow to separate from the inner bank and generate recirculating eddies on the lee side of the bend.

Flow separation can increase the drag in meanders through two mechanisms, i.e., increasing the bed shear stress and creating form drag across the bend. Flow separation can redistribute the streamwise momentum and thereby affect the bottom stress in the bend. In the plan view, the maximum depth-averaged velocity occurs near the inner bank in a bend with laterally uniform bathymetry as a result of Bernoulli effect (e.g., Leopold 1960; Blanckaert 2015; Kranenburg et al. 2019). When flow separation occurs downstream of the bend apex, the maximum velocity detaches from the inner bank and shifts toward the center of the channel (Leopold 1960; Vermeulen et al. 2015). The main flow is restricted to a narrower part of the cross section by the recirculating separation zone and is thus accelerated. The bottom friction is locally enhanced in regions with the accelerated flow and reduced in the low-velocity separation zone. As a result, the overall bed shear stress increases in the bend with flow separation because of the quadratic dependence of stress on velocity (Bo and Ralston 2020).

Moreover, flow separation can affect the large-scale momentum budget by creating form drag across the bend. The separation zone has a lower water level than the main flow, and the resulting pressure difference across the bend leads to form drag (Leopold 1960; McCabe et al. 2006; Bo and Ralston 2020). Form drag is the integrated pressure force normal to the channel boundaries, in contrast to bottom friction that results from shear near the bed. In an idealized modeling study, form drag was found to be the dominant contributor to drag increase in sinuous estuarine channels, especially in sharp bends (Bo and Ralston 2020). Observations from sinuous tidal channels have found effective C_d values in the range of 0.02–0.03 and more than twice greater than attributable to bed shear stress alone (Bo et al. 2021; Ortals et al. 2021), implying that form drag can cause a major increase in the total drag in natural channels.

In sinuous channels, all the abovementioned mechanisms can potentially contribute to the drag increase, including vertical and lateral advection of momentum by secondary circulation, lateral squeezing of channel flow by the recirculating zone, and form drag created by flow separation. In this study, we use a realistic model of the North River estuary (Massachusetts, United States) to quantitatively diagnose the influences of curvature-induced processes on the momentum budget and drag force in channel bends. The North River estuary is a sinuous tidal channel (Kranenburg et al. 2019; Bo et al. 2021; Garcia et al. 2022) and the present research focuses on the midestuary region with several channel bends. High drag was observed in this region, and both the curvature-induced secondary circulation and flow separation were suggested as sources of the high drag (Bo et al. 2021). Idealized simulations inspired by the North River indicate that form drag due to flow separation can be the dominant source of drag increase in sharp idealized bends (Bo and Ralston 2020), but the idealized

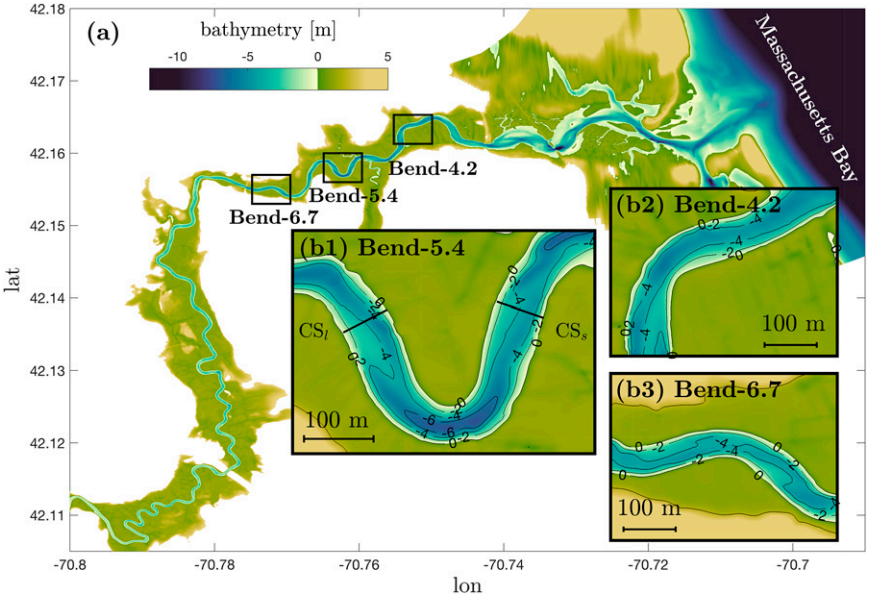

FIG. 1. Model bathymetry. (a) The North River estuary. (b1) Bend-5.4 (the sharp bend) at 5.4 km into the estuary. The landward control surface CS_l and seaward control surface CS_s show the domain selected for drag calculation. (b2),(b3) Bend-4.2 (intermediate sharpness) at 4.2 km and Bend-6.7 (smooth) at 6.7 km into the estuary, respectively.

model geometry did not include the bathymetric heterogeneity found in most natural systems. While the mechanisms of how secondary circulation affects drag have been brought up by several studies (Chang 1984; Seim et al. 2002; Blanckaert and de Vriend 2003; Blanckaert and Graf 2004), a thorough assessment of the processes in natural meanders is lacking. Here we use the realistic North River model to evaluate directly the processes that contribute to drag increase in estuarine meanders, including secondary circulation and flow separation.

In section 2, we introduce the realistic North River estuary model. Section 3 presents the overall estuarine conditions, flow patterns in meanders, and the calculated drag coefficient. In section 4, we evaluate different sources of drag increase and investigate the underlying mechanisms. In section 5, we discuss the broader application of the results and their implications for meander morphodynamics. Section 6 is a conclusion.

2. Methods

a. Field site

The North River estuary is a sinuous tidal channel through a salt marsh (Fig. 1a). The region of interest is the midestuary of the North River (~3–7 km from the mouth), where the channel width W is around 50 m and depth H is around 5 m, i.e., an aspect ratio W/H of 10, which is common for salt marsh meanders (Marani et al. 2002). The radius of curvature R ranges between 60 and 200 m, yielding a curvature ratio R/W of around 1.2–4. The ratio R/W is typically in the range of 1–5 in river and tidal meanders (Leopold and Wolman 1960; Marani et al. 2002), so the bend sharpness of the North River is representative of other sinuous channels in nature. Most of the analysis presented here focuses on a relatively sharp bend at 5.4 km into the estuary (Bend-5.4 in Fig. 1b1). Bend-5.4 has an $R/W \approx 1.2$, which is at the lower end of the range of typical values but similar to R/W for bends in other systems (e.g., Marani et al. 2002; Nanson 2010; Schnauder and Sukhodolov 2012). The channel is deeper near the bend apex and shallower at the crossover regions between bends, with shoals growing from the inner bank on the seaward side of Bend-5.4 and also on the seaward side of the next bend landward. While shallow point bars are found at the inner bank in many fluvial bends, the cross-channel bathymetry near the apex of bends in the North River is typically symmetric with steep banks and no distinct point bar. The analysis here also examines two bends that are less sharp at 4.2 km (Bend-4.2 in Fig. 1b2, intermediate sharpness, $R/W \approx 2$) and 6.7 km (Bend-6.7 in Fig. 1b3, relatively smooth, $R/W \approx 4$) to assess variability with the curvature ratio.

Observational data were collected in the North River midestuary region from mid-April to late July in 2017 (Kranenburg et al. 2019; Bo et al. 2021). Five sets of conductivity–temperature–depth (CTD) sensors were deployed from 3 to 8 km, namely, Moor1–5 (see the supplemental material for details). Moor3 is located at the apex of Bend-5.4 (the sharp bend). Velocity profile data were collected by upward-looking acoustic Doppler current profilers deployed near bottom CTD sensors at Moor1, 3, and 5. These data are used for evaluation of the realistic North River model that is introduced next.

b. Numerical model of the North River estuary

The Regional Ocean Modeling System (ROMS) is used to simulate the North River estuary. ROMS is a free-surface hydrostatic model based on the Reynolds-averaged Navier–Stokes

(RANS) equations, with structured grids and terrain-following vertical coordinates (Shchepetkin and McWilliams 2005; Haidvogel et al. 2008; Warner et al. 2008, 2010). The model domain extends from around 6 km off the coast to 18 km into the estuary (Fig. 1a). An orthogonal curvilinear grid follows the marsh platform with the highest resolution of 3 m in the channel (around 10–30 grid cells across the channel) and increasing grid spacing in the ocean and over the marsh away from the channel.

The model has tidal and subtidal forcings on the open ocean boundary on the east side of the model domain. Tidal amplitudes were extracted from the ADCIRC database (Mukai et al. 2002), and subtidal fluctuations were obtained from the low-pass-filtered water surface elevation record from the National Oceanic and Atmospheric Administration (NOAA) station at Boston (8443970). River discharge input from the west side, with data from the U.S. Geological Survey (USGS) gauge at Hanover (01105730) multiplied by 2.3 to account for freshwater inputs below the gauge.

Model bathymetry was constructed by combining existing datasets and new surveys. Digital elevation data from the U.S. Geological Survey (USGS) Coastal National Elevation Database (CoNED) and the U.S. Army Corps of Engineers (USACE) Topobathy Lidar Dataset were used for the marsh platform, the North River mouth region, the South River, and the offshore areas in Massachusetts Bay. Surveys in the North River were conducted using unmanned surface vehicles with bathymetric sonar systems (Kimball et al. 2014; Francis and Traykovski 2021).

The model has 16 uniformly distributed vertical layers, and the k–ϵ closure of the generic length scale (GLS) vertical mixing scheme is used for the vertical turbulent mixing (Umlauf and Burchard 2003; Warner et al. 2005). The horizontal mixing coefficient is set to 0.01 $m^2\ s^{-1}$. The bottom roughness z_0 is 0.005 m and uniform in the domain, except that at around 7 km from the mouth, z_0 is locally increased to up to 0.2 m to represent a section with larger rocks on the bed. The Coriolis force is included in the model, and while Coriolis dominates the secondary circulation in some systems (e.g., Johnson and Ohlsen 1994; Ott and Garrett 1998; Lerczak and Geyer 2004), it is negligible in narrow estuaries like the North River.

The simulations focus on a neap-to-spring transition from 19 to 27 April in 2017. During the simulated period, the freshwater discharge was moderate to high (5–15 $m^3\ s^{-1}$, corresponding to a mean seaward velocity of 2–6 cm s^{-1} in the sharp bend), leading to intermittent stratification. Model results are compared with the observational data described above (Kranenburg et al. 2019; Bo et al. 2021). Model performance is assessed by calculating the Murphy skill score (Murphy 1988; Ralston et al. 2017)

$$\text{Skill} = 1 - \frac{\sum(X_{\text{model}} - X_{\text{obs}})^2}{\sum(X_{\text{obs}} - \overline{X_{\text{obs}}})^2}, \tag{5}$$

where X_{model} represents model predictions and X_{obs} represents observations with a time mean $\overline{X_{\text{obs}}}$. Skill = 1 has perfect agreement between the model results and observations, and a Skill of 0 has the root-mean-square error comparable to the standard deviation of the observations. Detailed results of the model evaluation are presented in section 2 and the supplemental material.

Based on comparison with time series of water level, velocity, and salinity at Moor1–5 along the estuary from observations in 2017 (Kranenburg et al. 2019; Bo et al. 2021), z_0 = 0.005 m is found to have the best overall model performance (see the sensitivity testing in the supplemental material). This value of z_0 is also consistent with the observed ripples and mega-ripples (~0.1-m amplitude and 1–10-m wavelength) commonly found on the North River bed (Bo et al. 2021).

c. *Drag coefficient C_d and bottom friction coefficient C_f*

The drag coefficient and bottom friction coefficient are used to quantify the momentum loss in the bend. We investigate the influence of different flow processes on the momentum budget and separate out their contributions to the drag by comparing three different definitions of the drag and friction coefficients: $C_{d,\text{xs}}$ is the drag coefficient based on the cross-sectional-average flux of along-channel momentum, $C_{f,\text{xs}}$ is the friction coefficient based on the cross-sectional-average flux, and $C_{f,H}$ is the friction coefficient based on the depth-average flux.

The coefficients $C_{d,\text{xs}}$ and $C_{f,\text{xs}}$ are both defined on cross-sectional-average flow properties. The drag coefficient $C_{d,\text{xs}}$ quantifies the total drag including bottom friction and form drag, while $C_{f,\text{xs}}$ only quantifies the bottom friction. The coefficient $C_{f,H}$ also quantifies the bottom friction but is defined based on the depth-average flow properties. Because of the spatial variations in channel bathymetry and flow field, the depth-average flow at different lateral locations may differ from the cross-sectional-average flow. Therefore, the friction coefficient could be sensitive to how it is defined, and $C_{f,H}$ and $C_{f,\text{xs}}$ can have different values and represent different physical meanings. Additional details are provided below and in section 4.

The depth-averaged along-channel momentum equation can be approximated as a balance between the tidal pressure gradient forcing and drag:

$$-\frac{1}{\rho}\frac{\partial \overline{p}}{\partial s} = \frac{\tau_t}{\rho H}, \tag{6}$$

where $\overline{p}$ is the depth-averaged pressure, s is the along-channel coordinate, τ_t is the total drag force, and H is water depth. While the advection term can be important locally, it is generally small at the bend-average scale (e.g., Seim et al. 2002; Rogers et al. 2018) and thus has been neglected in the bend-scale momentum budget examined here. The time rate of change term is also small as we mainly focus on periods away from slack water. The pressure gradient $\partial\overline{p}/\partial s$ results from both the water-level gradient and salinity gradient

$$-\frac{1}{\rho}\frac{\partial \overline{p}}{\partial s} = -g\frac{\partial \eta}{\partial s} - \frac{1}{2}\beta g\frac{\partial \overline{S}}{\partial s}H, \tag{7}$$

where η is the water level, $\overline{S}$ is the depth-averaged salinity, and β is the haline contraction coefficient. Substituting (1) and (7) into (6),

$$-g\frac{\partial \eta}{\partial s}-\frac{1}{2}\beta g\frac{\partial \overline{S}}{\partial s}H=\frac{C_d\overline{u}|\overline{u}|}{H}. \quad (8)$$

The momentum Eq. (8) is integrated through the bend to evaluate the overall drag, i.e.,

$$\int_0^L\int_0^W\left(-g\frac{\partial \eta}{\partial s}-\frac{1}{2}\beta g\frac{\partial \overline{S}}{\partial s}H\right)ds\,dr=\int_0^L\int_0^W C_d\frac{\overline{u}|\overline{u}|}{H}\,ds\,dr, \quad (9)$$

where r is the lateral coordinate, and L and W are the bend length and channel width, respectively. Averaging (9) over the bend scale, we can write a finite difference form of the momentum budget:

$$-g\frac{\Delta \eta}{L}-\frac{1}{2}\beta g\frac{\Delta S}{L}\{\langle H\rangle\}=\left\{\left\langle C_d\frac{\overline{u}|\overline{u}|}{H}\right\rangle\right\}, \quad (10)$$

where $\Delta\eta$ and ΔS are the water-level and salinity difference between the bend exit and entrance (laterally or cross-sectionally averaged), $\{\cdot\}$ represents the along-channel average through the bend, and $\langle\cdot\rangle$ represents the lateral average.

We define a cross-sectional-average drag coefficient $C_{d,\mathrm{xs}}$ for the bend based on the cross-sectional average velocity $\langle\overline{u}\rangle$ and lateral average depth $\langle H\rangle$:

$$\left\{\left\langle C_d\frac{\overline{u}|\overline{u}|}{H}\right\rangle\right\}=C_{d,\mathrm{xs}}\left\{\frac{\langle\overline{u}\rangle|\langle\overline{u}\rangle|}{\langle H\rangle}\right\}. \quad (11)$$

Therefore, $C_{d,\mathrm{xs}}$ is calculated as the pressure gradient across the bend divided by the bend-average of $\langle\overline{u}\rangle$ squared divided by $\langle H\rangle$, i.e.,

$$C_{d,\mathrm{xs}}=\frac{-g(\Delta\eta/L)-\frac{1}{2}\beta g(\Delta S/L)\{\langle H\rangle\}}{\{\langle\overline{u}\rangle|\langle\overline{u}\rangle|/\langle H\rangle\}}. \quad (12)$$

The cross-sectional-average drag coefficient $C_{d,\mathrm{xs}}$ represents the total effective drag for a given amount of volumetric flux Q through the bend, with $Q=\langle\overline{u}\rangle\langle H\rangle W$ for each cross section. Moreover, the volumetric flux Q is conserved through the bend, so by assuming no significant along-channel variability of the channel width and depth,

$$\left\{\frac{\langle\overline{u}\rangle|\langle\overline{u}\rangle|}{\langle H\rangle}\right\}=Q|Q|\left\{\frac{1}{\langle H\rangle^3W^2}\right\}\approx\frac{Q|Q|}{\{\langle H\rangle\}^3\{W\}^2}\approx\frac{\{\langle\overline{u}\rangle\}|\{\langle\overline{u}\rangle\}|}{\{\langle H\rangle\}}. \quad (13)$$

Thus, $C_{d,\mathrm{xs}}$ defined by (12) is similar to a bulk drag coefficient $C_{d,\mathrm{bulk}}$:

$$C_{d,\mathrm{bulk}}=\frac{-g(\Delta\eta/L)-\frac{1}{2}\beta g(\Delta S/L)\{\langle H\rangle\}}{\{\langle\overline{u}\rangle\}|\{\langle\overline{u}\rangle\}|/\{\langle H\rangle\}}. \quad (14)$$

The cross-sectional-average drag coefficient $C_{d,\mathrm{xs}}$ is based on the average of $\langle\overline{u}\rangle^2/\langle H\rangle$ through the bend, while the bulk drag coefficient $C_{d,\mathrm{bulk}}$ is a more straightforward definition by averaging $\langle\overline{u}\rangle$ and $\langle H\rangle$ separately through the bend. The bulk drag coefficient $C_{d,\mathrm{bulk}}$ is generally close to $C_{d,\mathrm{xs}}$ in the North River, where the channel cross-sectional area does not notably change with distance along-channel. However, $C_{d,\mathrm{bulk}}$ is not an applicable approximation of $C_{d,\mathrm{xs}}$ in systems with large streamwise variations in depth and velocity, e.g., the flow over coral reefs in Lentz et al. (2017), so we use (12) to quantify the overall drag in this study.

Similar to the cross-sectional-average drag coefficient $C_{d,\mathrm{xs}}$ that quantifies the total drag, we define a cross-sectional-average bottom friction coefficient $C_{f,\mathrm{xs}}$ that quantifies the effective bottom friction in the bend but not the form drag.

$$C_{f,\mathrm{xs}}=\frac{\{\langle\tau_b/(\rho H)\rangle\}}{\{\langle\overline{u}\rangle|\langle\overline{u}\rangle|/\langle H\rangle\}}, \quad (15)$$

with τ_b being the bottom shear stress.

Since the drag varies with $\overline{u}^2$ and $1/H$, the lateral variations in each of them can nonlinearly affect the total drag in ways that are not represented in the cross-sectional average velocity and depth. Therefore, a depth-average drag coefficient $C_{d,H}$ based on the local depth H and depth-averaged velocity $\overline{u}$ can be defined to account for this spatial variability:

$$\left\{\left\langle C_d\frac{\overline{u}|\overline{u}|}{H}\right\rangle\right\}=C_{d,H}\left\{\left\langle\frac{\overline{u}|\overline{u}|}{H}\right\rangle\right\}. \quad (16)$$

In this research, $C_{d,H}$ is not calculated, because there is form drag in the bend which has to be calculated as a spatial integral over the topographic feature of interest and cannot be estimated locally (McCabe et al. 2006; Bo and Ralston 2020). Instead, we use the depth-average bottom friction coefficient $C_{f,H}$ that quantifies bottom shear stress alone:

$$C_{f,H}=\frac{\{\langle\tau_b/(\rho H)\rangle\}}{\{\langle\overline{u}|\overline{u}|/H\rangle\}}. \quad (17)$$

The friction coefficients $C_{f,H}$ and $C_{f,\mathrm{xs}}$ both have the bend-average bottom shear stress on the numerator, and the difference lies in the denominator term (velocity squared divided by depth) used to nondimensionalize the drag. The depth-average bottom friction coefficient $C_{f,H}$ quantifies the bend-average bottom friction experienced by the locally varying flow, while $C_{f,\mathrm{xs}}$ represents the overall effective bottom friction experienced by the cross-sectional average flux in the bend. As an example, in a straight channel with complex bathymetry, $C_{f,H}$ will be close to values estimated by (4) when a stable log profile is established everywhere, but $C_{f,\mathrm{xs}}$ can be increased due to correlations between spatially variable velocity and depth, e.g., when strong currents occur in shallow regions of the channel. It is also worthwhile to note that $C_{f,H}$ is usually difficult to estimate in the field given the requirement of high spatial resolution measurements of velocity and depth, but this definition is necessary to assess the influence of the horizontal variations in the flow field on the drag. The calculation of $C_{f,\mathrm{xs}}$ is more achievable in the field with a knowledge of channel bathymetry and an estimation of the volumetric flux in a representative cross section.

3. Results

a. Estuarine conditions and model evaluation

The North River estuary is dominantly forced by semidiurnal tides and during the observation period the tide range

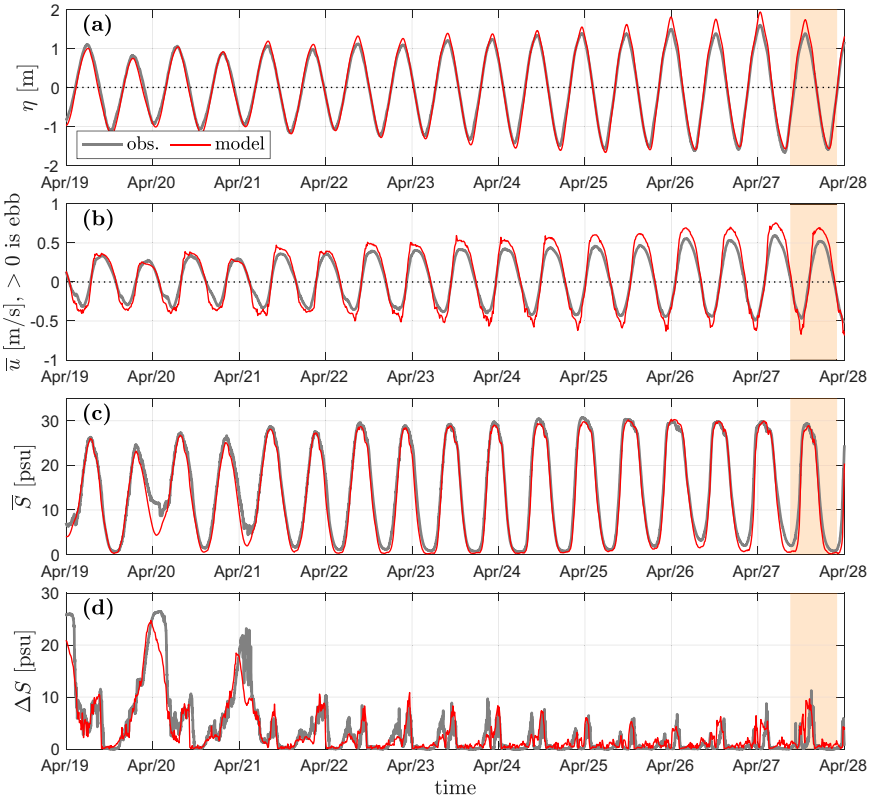

FIG. 2. The modeled estuarine conditions compared with observations at Moor3 (at the apex of Bend-5.4) in April 2017. Thick gray lines represent observations, and thin red lines represent model results. (a) Water level η. (b) Depth-averaged velocity $\overline{u}$. (c) Depth-averaged salinity $\overline{S}$. (d) Stratification ΔS (bottom-surface salinity difference). Orange bands show the tidal cycle selected for detailed analysis.

varied between around 2 m (19 April, neap tide) and 3 m (27 April, spring tide) (Fig. 2). The maximum tidal current in Bend-5.4 that is the focus of this study is around 0.5–0.8 m s^{-1}. Generally stratification is stronger during neap tides (instantaneous bottom-surface salinity difference ΔS up to ~20 psu) and weaker during spring tides (ΔS up to ~5 psu). Stratification also has significant intratidal variations due to the along-estuary advection of salinity gradient by the tidal currents. In the midestuary, stratification mainly occurs from late flood tide to early ebb tide.

A tidal cycle on 27 April is selected for detailed analysis in the following sections as a representative of weakly stratified conditions (Fig. 2d). We mainly focus on periods around maximum tidal velocity when the drag is greatest. Stratification is weak around the times of maximum tidal currents for most of the spring–neap cycle, except during the weakest neap tides. In addition, discharge in the North River was relatively high during the observations in late April. Discharge is generally lower during other seasons, and thus stratification is weaker than during the study period. The following results and analysis mainly focus on periods with weak stratification, and the effects of stronger stratification will be discussed in section 5.

The model results are compared with observations, indicating an overall good model performance. At Moor3 (at the apex of Bend-5.4) skill scores are Skill = 0.98 for water level and Skill = 0.97 for salinity. Comparisons of velocity and stratification yield Skill = 0.91 and Skill = 0.82, respectively, which are slightly lower and more sensitive to the measurement location compared to the other two variables. Assessments of model performance at moorings located in other parts of the estuary are shown in the supplemental material and generally have similar skill scores to Moor3.

b. *Secondary circulation and flow separation*

Two key flow processes, i.e., secondary circulation and flow separation, influence the momentum budget and drag in meanders. Thus, in this section, we present the flow patterns in Bend-5.4 where observations have previously been made (Kranenburg et al. 2019; Bo et al. 2021) and assess the influence of secondary circulation and flow separation on momentum distribution. The influences of curvature on drag also apply to other bends along the estuary, and those results are presented in a later section.

During the ebb tide, the classical helical flow develops in Bend-5.4 (Figs. 3 and 5a,b), with inward secondary flow near the bed and outward flow near the surface. The maximum streamwise velocity occurs near the inner bank as flow approaches the bend apex (XS1 in Fig. 5a), as a result of the

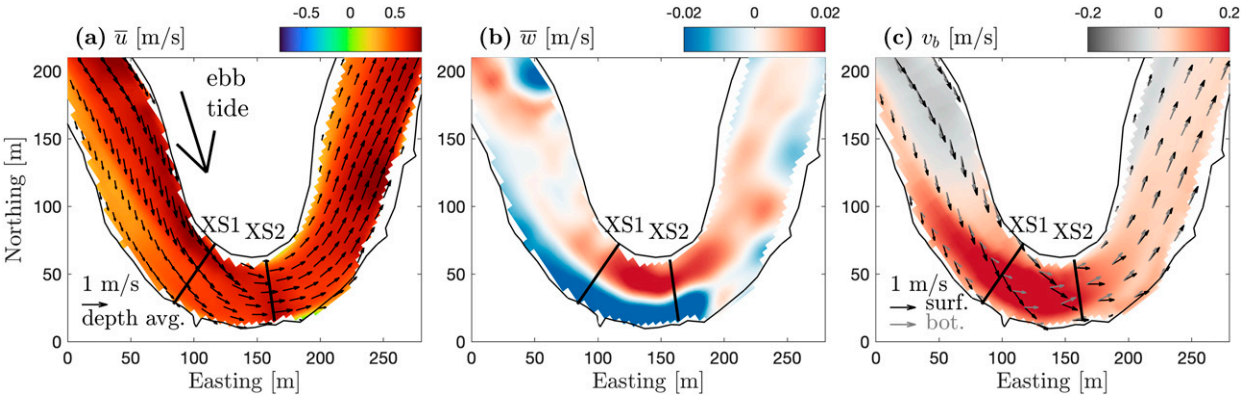

FIG. 3. The ebb tide flow field in Bend-5.4 (at 3 h after slack water). (a) Depth-averaged streamwise velocity $\overline{u}$. Positive u means seaward velocity (ebb direction). Arrows show the depth-averaged horizontal velocity. (b) Depth-averaged vertical velocity $\overline{w}$. (c) Near-bed lateral velocity v_b. Positive means inward in the focused bend (approximately northward). Black arrows represent the surface velocity, and gray arrows represent the bottom velocity.

Bernoulli effect (e.g., Leopold 1960; Blanckaert 2015; Kranenburg et al. 2019). The outward lateral flow tends to advect the higher momentum toward the outer bank in the upper water column, and the vertical velocity near the outer bank transports higher momentum flow downward and increases the streamwise velocity near the bed. The higher momentum flow then is spread laterally inward by the secondary flow near the bed. As a result of the stirring (lateral and vertical advection) by secondary circulation, the streamwise velocity, which is concentrated near the surface at the inner bank upstream in the bend, becomes more uniformly distributed in the cross section near the bend apex (XS2 in Fig. 5b). Maximum velocities in vertical profiles appear near the bed in the outer bend at the bend apex, similar to velocity profiles reported in laboratory studies of bends with uniform density and laterally uniform bathymetry (e.g., Blanckaert and Graf 2004).

During the flood tide, the flow structures are different from the classical helical flow in meanders due to flow separation and more complex secondary circulation. The main flow detaches from the inner bank at the bend apex, with zero and even reversed streamwise velocity near the inner bank (Fig. 4a). Flow separation leads to the generation of horizontal vorticity (Fig. 4d), and a recirculating eddy occurs in the separation zone on the lee side of the bend. Similar flow separation has been reported in laboratory bends (e.g., Leopold 1960; Blanckaert 2015), idealized sinuous channels (e.g., Bo and Ralston 2020), natural rivers (e.g., Ferguson et al. 2003; Frothingham and Rhoads 2003), and tidal channels (e.g., Leeder and Bridges 1975) including the North River estuary (Bo et al. 2021).

While the maximum streamwise velocity is near the inner bank upstream of the bend apex (XS3 in Fig. 5c), the region with maximum along-channel momentum is shifted toward the center of the channel where flow separation occurs (XS4 in Fig. 5d). In addition, a low velocity zone is found near the outer bank upstream of the bend apex (XS3 in Fig. 5c), indicating flow separation near the outer bank. The outer bank separation occurs due to an adverse pressure gradient along the outer bank approaching the bend apex and is analogous to the inner bank flow separation downstream of the apex (Blanckaert 2010; Blanckaert et al. 2013; Vermeulen et al. 2015). Outer bank separation can also squeeze and accelerate the main flow, although it is less commonly found in the North River model than inner bank separation.

In contrast to the classical curvature-induced secondary circulation during the ebb tide, multiple secondary circulation cells occur during the flood tide. This more complex secondary circulation appears due to the combined effect of channel curvature and salinity variations during floods, as was investigated by an observational study in this bend (Kranenburg et al. 2019). Upstream of the bend apex (XS3 in Fig. 5c), the laterally sheared along-channel velocity creates a lateral density difference through differential advection of the along-channel salinity gradient (Kranenburg et al. 2019), with saltier water and the maximum velocity near the inner bank. The resulting lateral baroclinic pressure gradient (BCPG) creates a primary secondary circulation cell in the outer part of the bend and a smaller cell near the inner bank, with surface convergence in between the cells at the streamwise velocity maximum (also see Fig. 4c). High momentum flow is transported to the lower water column by the downward velocity at the surface convergence and spreads laterally near the bed with the lateral velocity. Downstream of the bend apex flow separation occurs (XS4 in Fig. 5d) and the secondary circulation becomes more complex, but the higher momentum streamwise flow remains in the lower water column.

c. *Drag and friction coefficients*

The cross-sectional-average drag coefficient $C_{d,\mathrm{xs}}$, cross-sectional-average bottom friction coefficient $C_{f,\mathrm{xs}}$, and depth-average bottom friction coefficient $C_{f,H}$ are calculated through Bend-5.4 for the neap-to-spring transition from 19 to 27 April. The control volume is selected as the channel between the bend crossovers (marked by two solid lines CS_l and CS_s in Fig. 1b1), excluding the marsh platform. The calculation is based on the model output of every 10 min, and we focus on ~2-h periods around maximum flood and ebb when the drag

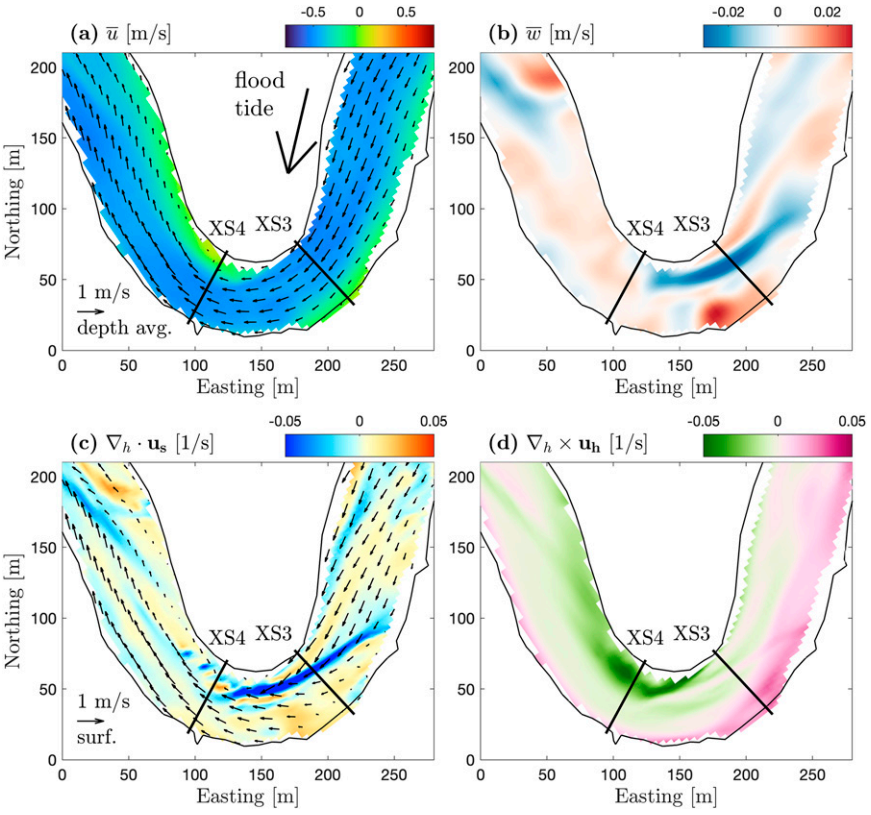

FIG. 4. The flood tide flow field in Bend-5.4 (at 3 h after slack water). (a) Depth-averaged streamwise velocity $\overline{u}$. Negative u means landward velocity (flood direction). Arrows show the depth-averaged horizontal velocity. (b) Depth-averaged vertical velocity $\overline{w}$. (c) Surface divergence $\nabla_h \cdot \mathbf{u}_s$. Arrows show $\mathbf{u}_s$, the surface horizontal velocity vector. Blue color means surface convergence. (d) Depth-averaged vertical vorticity $\nabla_h \times \mathbf{u}_h$, with $\mathbf{u}_h$ being the depth-averaged horizontal velocity vector.

is greatest. During several of the strongest spring tides, the water level exceeds the bank height and the marsh is inundated from maximum flood tide to early ebb, and these periods are not included in the calculation.

The calculated $C_{d,\mathrm{xs}}$, $C_{f,\mathrm{xs}}$, and $C_{f,H}$ are plotted as a function of water depth H (Fig. 6a). Note that the water depth is greater during flood tides than ebb tides because the phase difference between tidal water level and velocity is less than 90°. The depth dependence is examined because both previous research on flow separation (Bo and Ralston 2020) and the classical solution to bottom boundary layer flow (4) suggest a dependence of drag on water depth. Assuming a log profile for streamwise velocity, the corresponding friction coefficient [from (4), hereby named as $C_{f,\log}$] is in the range of 0.004–0.005 for $z_0 = 5$ mm and a depth of 3–6 m. The $C_{f,\log}$ decreases as water depth increases for channel flow with log profiles because the velocity profile becomes less sheared in the upper water column with increasing flow depth (e.g., Bricker et al. 2005; Lentz et al. 2017). The calculated $C_{d,\mathrm{xs}}$, $C_{f,\mathrm{xs}}$, and $C_{f,H}$ are all greater than the value of $C_{f,\log}$ from the log-profile assumption, with the exception of some stratified cases that will be discussed later. The greater values are consistent with the observed high drag in the North River estuary (Bo et al. 2021) and reflect the increase in drag due to channel curvature. The total drag $C_{d,\mathrm{xs}}$ can be up to a factor of 2 larger than the $C_{f,\mathrm{xs}}$ due to bottom friction alone, suggesting that form drag due to flow separation sometimes dominates the additional momentum loss (Bo and Ralston 2020). The $C_{f,\mathrm{xs}}$ and $C_{f,H}$ are also greater than the typical values of 0.004–0.005, indicating that the bottom shear stress is enhanced in the bend. In addition, the calculated $C_{d,\mathrm{xs}}$, $C_{f,\mathrm{xs}}$, and $C_{f,H}$ in the bend display more complex depth dependence compared to $C_{f,\log}$, because of various contributing factors to the drag. In the following section, the contributions of the secondary circulation, form drag, and streamwise velocity distribution to enhancing the drag with flow curvature will be diagnosed through analysis of the different drag and friction coefficients.

4. Analysis

a. *Identifying sources of drag increase*

1) FORM DRAG

The cross-sectional-average drag coefficient $C_{d,\mathrm{xs}}$ is around 0.008–0.013, and the cross-sectional-average bottom friction coefficient $C_{f,\mathrm{xs}}$ is 0.006–0.008. The ratio of $C_{d,\mathrm{xs}}/C_{f,\mathrm{xs}}$

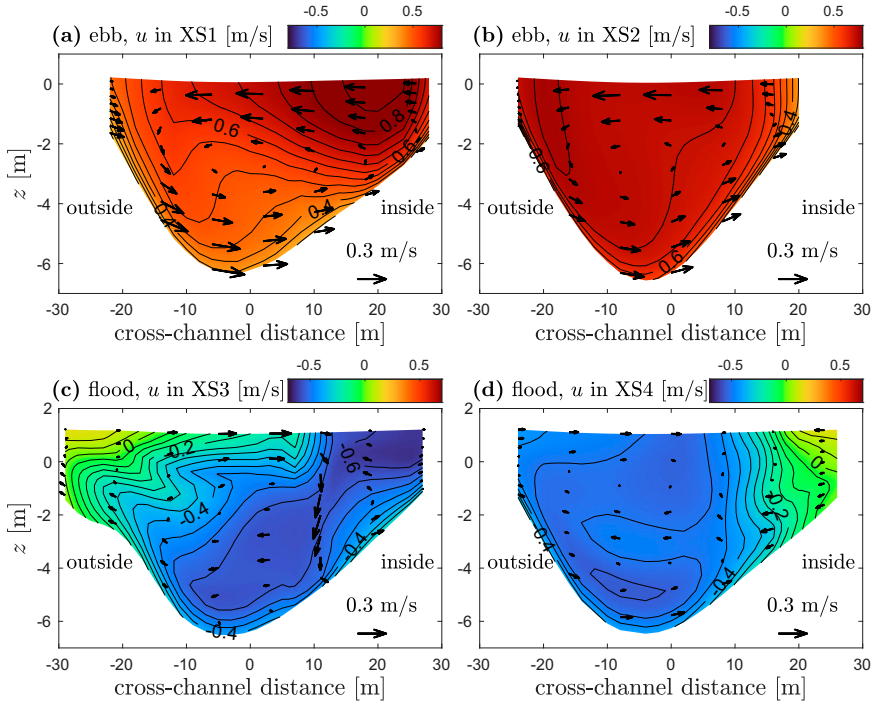

FIG. 5. (a),(b) Along-channel velocity u in the cross sections XS1 and XS2 during the ebb tide. Locations of XS1 and XS2 are marked in the map views in Fig. 3. (c),(d) Along-channel velocity u in the cross sections XS3 and XS4 during the flood tide. The locations of XS3 and XS4 are marked in the map views in Fig. 4. Positive u means seaward velocity (ebb direction), and negative u means landward velocity (flood direction).

compares the contribution of form drag versus bottom friction in the bend (Fig. 6b), and it indicates a total drag increase of up to 80% due to the form drag. Flow separation can create a low-pressure recirculation zone on the lee side of the bend, and the resulting pressure difference across the bend leads to a net pressure force exerted by the channel boundaries on the flow, i.e., the form drag. Form drag has been suggested to be a dominant source of drag in the North River estuary based on previous observations Bo et al. (2021). Form drag was directly calculated in idealized models that scaled with the North River and it accounted for the difference between the total momentum loss and bottom friction (Bo and Ralston 2020). The complex geometry and bathymetry of the realistic model here make the direct calculation of form drag prohibitively difficult. Nonetheless, the characteristics of the flow and the excess water-level drop that is not balanced by the bottom friction clearly indicate the dominance of form drag in this situation.

Form drag is most notable during flood tides and can increase the drag by 50%–80% compared to bottom friction alone. During ebb tides, form drag is smaller and even negligible. This flood–ebb asymmetry in form drag is consistent with the above-described flow field in the bend (section 3b), where flow separation is mainly found during floods. Flow separation typically occurs as a result of the adverse pressure gradient along the inner bank downstream of the bend apex (Blanckaert 2010; Vermeulen et al. 2015; Bo and Ralston 2020). While the curvature effect tends to set an adverse pressure gradient behind the bend that can lead to flow separation, bottom friction in the channel sets a favoring pressure gradient that can inhibit flow separation (Signell and Geyer 1991; Bo and Ralston 2020). An adverse pressure gradient occurs when the curvature effect exceeds the frictional effect, resulting in flow separation in the lee of a bend.

We investigate the along-inner-bank water-level distribution to understand the flood–ebb asymmetry in flow separation and form drag (Fig. 7). During early flood tide, the lowest water level is found near the bend apex on the inner bank, with an adverse pressure gradient along the inner bank downstream of the apex. As a result, flow separation develops later into flood tide and a low-pressure recirculation zone grows downstream. The low-pressure zone on the lee sidewall results in a pressure difference across the bend, thus creating form drag. By contrast, a favoring pressure gradient along the inner bank persists during the ebb tide, and without an adverse pressure gradient flow separation and form drag do not occur.

The flood–ebb asymmetry in adverse pressure gradients, flow separation, and form drag can be partially explained by a depth dependence. The water is deeper during flood tides, so the inertial effect of curved flows has greater influence on setting an adverse pressure gradient and reversing the flow direction (Bo and Ralston 2020). However, during ebb tides the tidal stage is lower and with shallower water a stronger

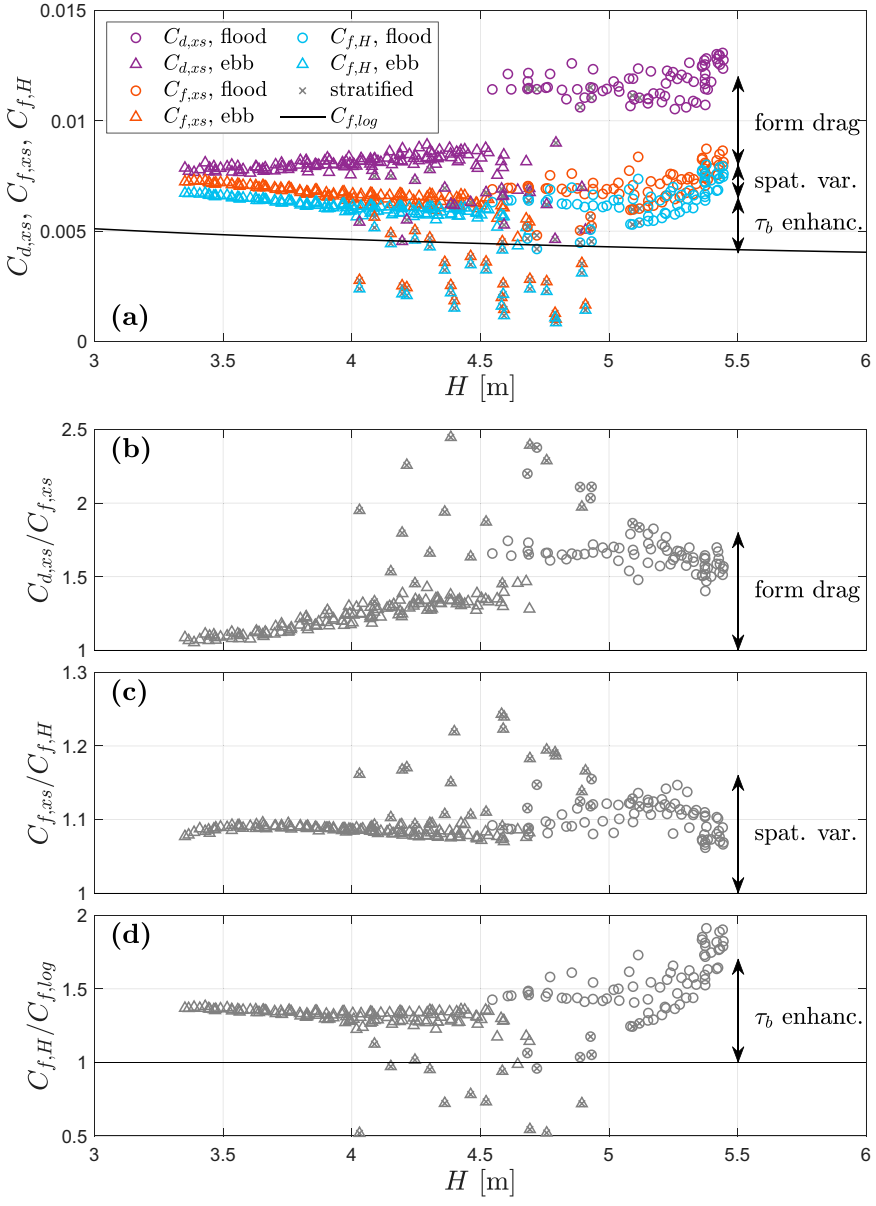

FIG. 6. The calculated cross-sectional-average drag coefficient $C_{d,\mathrm{xs}}$, cross-sectional-average friction coefficient $C_{f,\mathrm{xs}}$, depth-average friction coefficient $C_{f,H}$, and their ratios as a function of water depth H in Bend-5.4. $C_{f,\mathrm{log}}$ is calculated from the log-profile assumption (4). Triangles represent ebb tide and circles represent flood tide. Stratified cases are marked by crosses, defined based on $\Delta S > 2$.

frictional effect tends to inhibit flow separation. The ratio of $C_{d,\mathrm{xs}}/C_{f,\mathrm{xs}}$ in the bend increases with water depth (Fig. 6b), which is consistent with the depth dependence of form drag with flow separation (Bo and Ralston 2020).

While the ratio of $C_{d,\mathrm{xs}}/C_{f,\mathrm{xs}}$ displays a more continuous depth dependence (Fig. 6b), the value of $C_{d,\mathrm{xs}}$ shows a larger gap between flood and ebb tides that cannot be explained by the difference in depth alone (Fig. 6a). We speculate that the distinct 3D flow structure during flood tides favors the onset of flow separation compared to ebb tides and enhances the flood–ebb asymmetry of form drag. During flood tides downwelling occurs near the inner bank upstream of the bend apex as a result of the BCPG-driven secondary circulation (Figs. 4b and 5c). The secondary flow tends to maintain high streamwise momentum with a convergence zone near the inside of the bend. This increased streamwise momentum enhances the water-level setdown at the bend apex due to the Bernoulli effect and favors the creation of an adverse pressure gradient downstream of the bend apex that can lead to flow separation (Fig. 7). Additionally, the downwelling near the

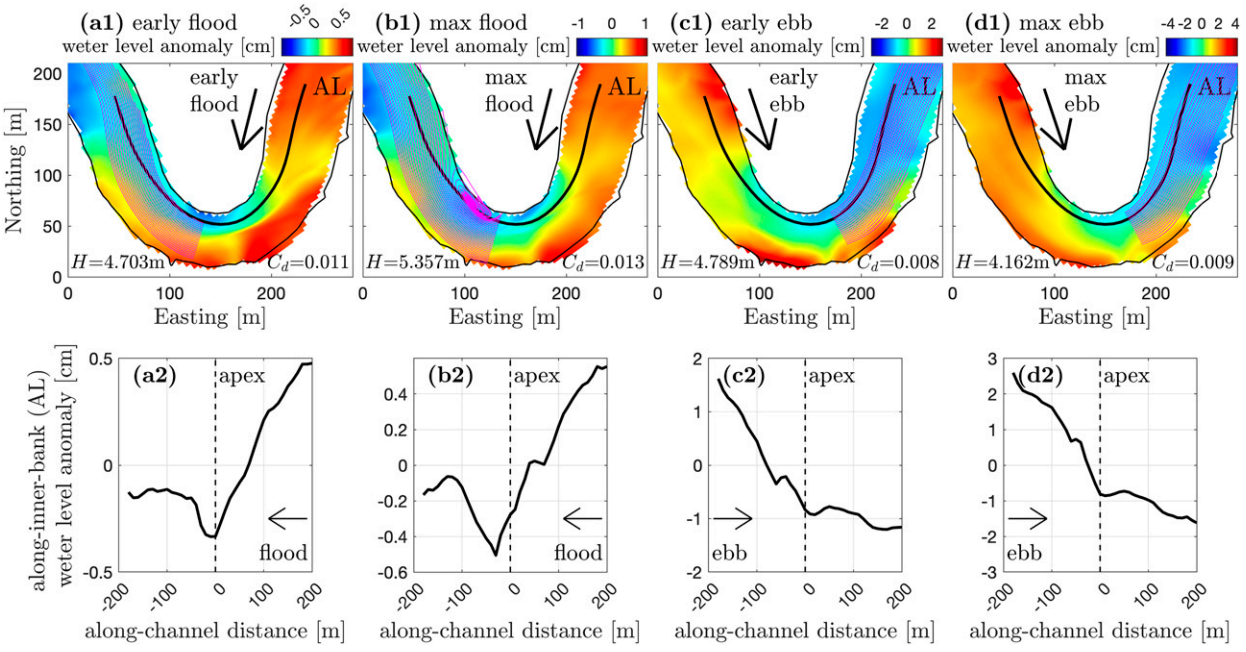

FIG. 7. Water-level anomaly in Bend-5.4. (a1) early flood tide (1 h after slack water); (b1) max flood tide (3 h after slack water); (c1) early ebb tide (1 h after slack water); (d1) max ebb tide (3 h after slack water). Magenta lines show streamlines starting from slightly downstream of the bend apex. Note that the streamlines are calculated based on the depth-averaged velocity field, and they only approximate the 3D channel flow. The water level slightly exceeds the bank height at this max flood tide, so some streamlines are terminated at the marsh platform. (a2)–(d2) Water-level anomaly on an along-inner-bank line (AL). The location of AL is marked in the map views.

inside of the bend during floods alters the vertical structure of streamwise velocity, with low velocity and reversed vertical shear in the upper column. Consequently, the influence of the bottom boundary layer is restricted to the lower water column (detailed analysis presented in section 4b), and the tendency of bottom friction to inhibit flow separation is suppressed. Therefore, the frictional effect is weakened by the BCPG-driven secondary circulation during flood tides compared to that expected based on water depth alone, and this enhances the flood–ebb asymmetry of flow separation and form drag. By comparison, river meanders typically have helical flows similar to the ebb tide cases in our study, and flow separation is not commonly found in rivers except in distinctly deep and sharp river bends (e.g., Ferguson et al. 2003; Schnauder and Sukhodolov 2012).

2) INCREASED OVERALL BOTTOM FRICTION DUE TO THE SPATIAL VARIABILITY OF FLOW FIELD

The ratio of cross-sectional-average to depth-average bottom friction coefficient $C_{f,xs}/C_{f,H}$ represents the drag increase due to the spatial variability of the velocity and water depth and their nonlinear correlation. The ratio $C_{f,xs}/C_{f,H}$ is essentially the ratio of $\{\langle\overline{u}|\overline{u}|/H\rangle\}/\{\langle\overline{u}\rangle|\langle\overline{u}\rangle|/\langle H\rangle\}$ [also see (15) and (17)], i.e., the spatial average of the local depth-average velocity squared divided by depth versus the cross-sectional average velocity squared divided by the lateral average depth. The ratio $C_{f,xs}/C_{f,H}$ is generally larger when higher velocities occur in shallower depths, i.e., more high local $\overline{u}|\overline{u}|/H$. For a given volume flux through the channel, the nonuniform bathymetry and resulting spatially variable velocity field can be nonlinearly correlated and lead to increased momentum loss compared to a uniform channel, even in the absence of additional factors like secondary circulation and flow separation. This part of drag increase is defined as the drag increase due to the spatial variability in streamwise velocity and water depth and is quantified by $C_{f,xs}/C_{f,H}$.

The $C_{f,xs}/C_{f,H}$ in this bend indicates a 10% drag increase during ebb tides and up to 15% increase during flood tides. The $C_{f,xs}/C_{f,H}$ can be slightly greater during flood tides because the curvature effect redistributes streamwise velocity such that faster flow occurs over shallow shoals. For example, maximum velocity usually occurs near the inner bank upstream of the bend apex (seaward for flood tide), which also is the location of a shallow shoal. The maximum velocity is shifted toward the outer bend by flow separation downstream of the bend apex and encounters a shallow shoal leading into the next bend landward (Figs. 1b1 and 4a). In comparison, during ebb tides higher velocity usually follows the deeper part of the channel and flow is weaker over the shoals (Fig. 3a). Tidal velocities in the North River are ebb dominant (Kranenburg et al. 2019), so ebb currents are expected to dominate the morphological development and the channel would be deeper where ebb currents are stronger.

3) ENHANCED LOCAL BOTTOM FRICTION DUE TO DEVIATION FROM THE LOG-PROFILE

The cross-sectional-average bottom friction coefficient $C_{f,H}$ is generally 0.005–0.007, greater than the log-profile prediction

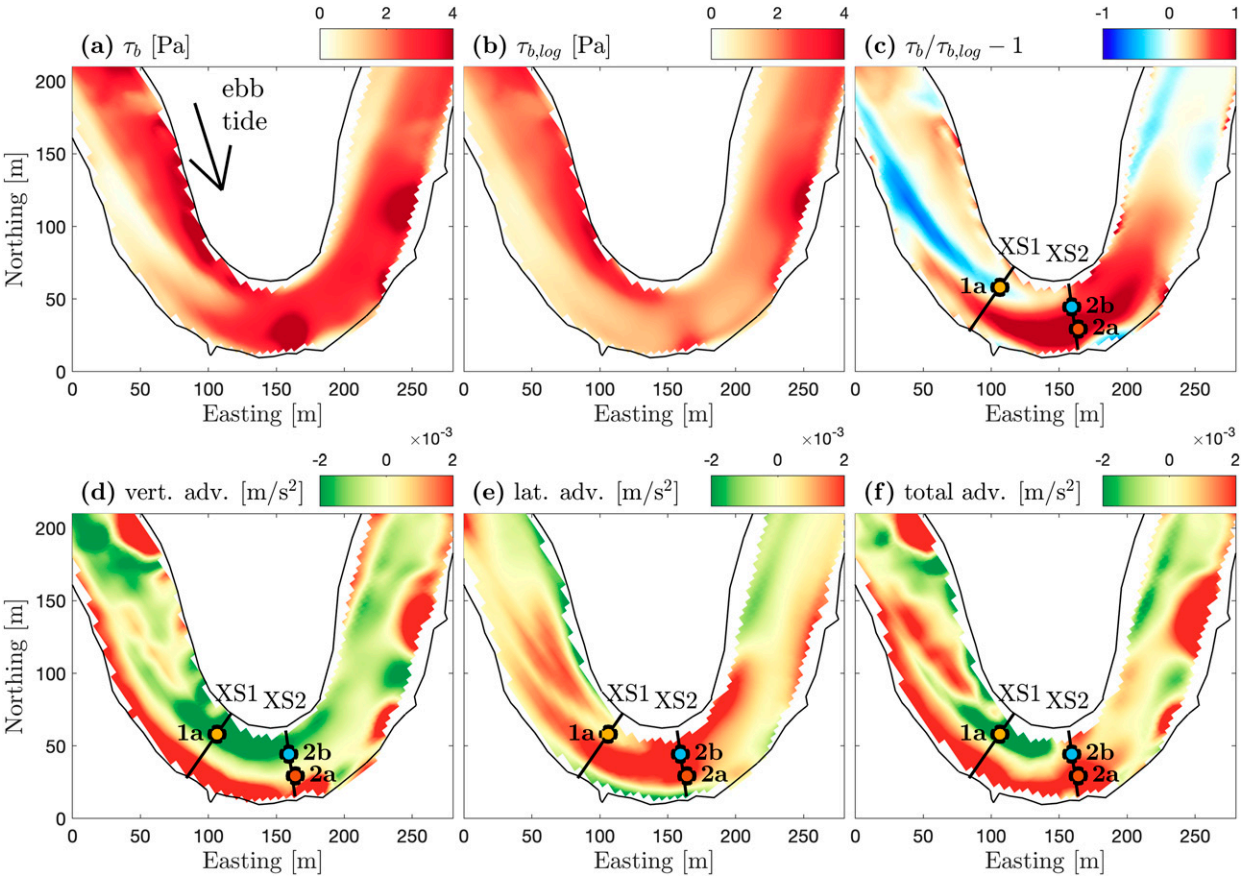

FIG. 8. The ebb tide bottom stress and momentum redistribution terms in Bend-5.4. (a) Bottom stress τ_b. (b) Predicted bottom stress $\tau_{b,\log}$ based on the log-profile assumption. (c) Relative difference between τ_b and $\tau_{b,\log}$. (d)–(f) The vertical, lateral, and total advection terms of along-channel velocity in (18).

$C_{f,\log}$ of 0.004–0.005. The ratio of $C_{f,H}/C_{f,\log}$ represents the local bed shear stress enhancement due to deviation from the log profile. The $C_{f,H}/C_{f,\log}$ indicates a 30%–40% drag increase during ebb tides and around 50% increase during flood tides compared to the log-profile assumption. This local bottom stress enhancement can be a dominant source of drag increase during ebb tides when flow separation and form drag do not occur. The enhancement of bottom shear stress relative to the log-profile assumption (4) suggests an alteration to the vertical profile of velocity. Secondary circulation in the bend can redistribute momentum in the cross sections through vertical and lateral advection, and thus enhance the bottom shear stress. Note that in some stratified cases $C_{f,H}$ may be decreased compared to $C_{f,\log}$, because stratification can inhibit turbulence and reduce the bottom shear stress (e.g., Turner and Turner 1979; Friedrichs and Wright 1997; Stacey and Ralston 2005).

It is also worthwhile to note that flow curvature results in two types of momentum redistribution in the bend. One is the redistribution of depth-averaged velocity in the horizontal plane, which is mainly related to the lateral squeezing of the main flow by flow separation. This generally increases the spatial variability of the depth-average flow field and the magnitude of the stress relative to the cross-sectionally averaged velocity, thus increasing the ratio $C_{f,xs}/C_{f,H}$ by ~10%. The other type of momentum redistribution is the alteration of the velocity profile in the vertical, which is mainly due to the vertical and lateral advection by the secondary circulation. This can cause a deviation from the log profile and thus affect the local bottom shear stress, and it is reflected in $C_{f,H}/C_{f,\log}$ that represents a greater increase of ~40%. This redistribution of streamwise flow in the vertical by the secondary circulation and its influence on the drag is investigated in the following section.

b. *Momentum redistribution and local bottom friction enhancement*

1) EBB TIDE

During ebb tide when the classical helical flow occurs in the bend, the bottom shear stress distribution primarily depends on the depth-averaged streamwise velocity (Figs. 3a and 8a), e.g., maximum bottom stresses occur near the inner bank upstream of the bend apex where maximum velocity occurs, and this shifts toward the outer bank downstream of the bend apex as higher momentum flow is transported outward. We calculated the expected bottom stress from the depth-averaged velocity and the log-profile assumption

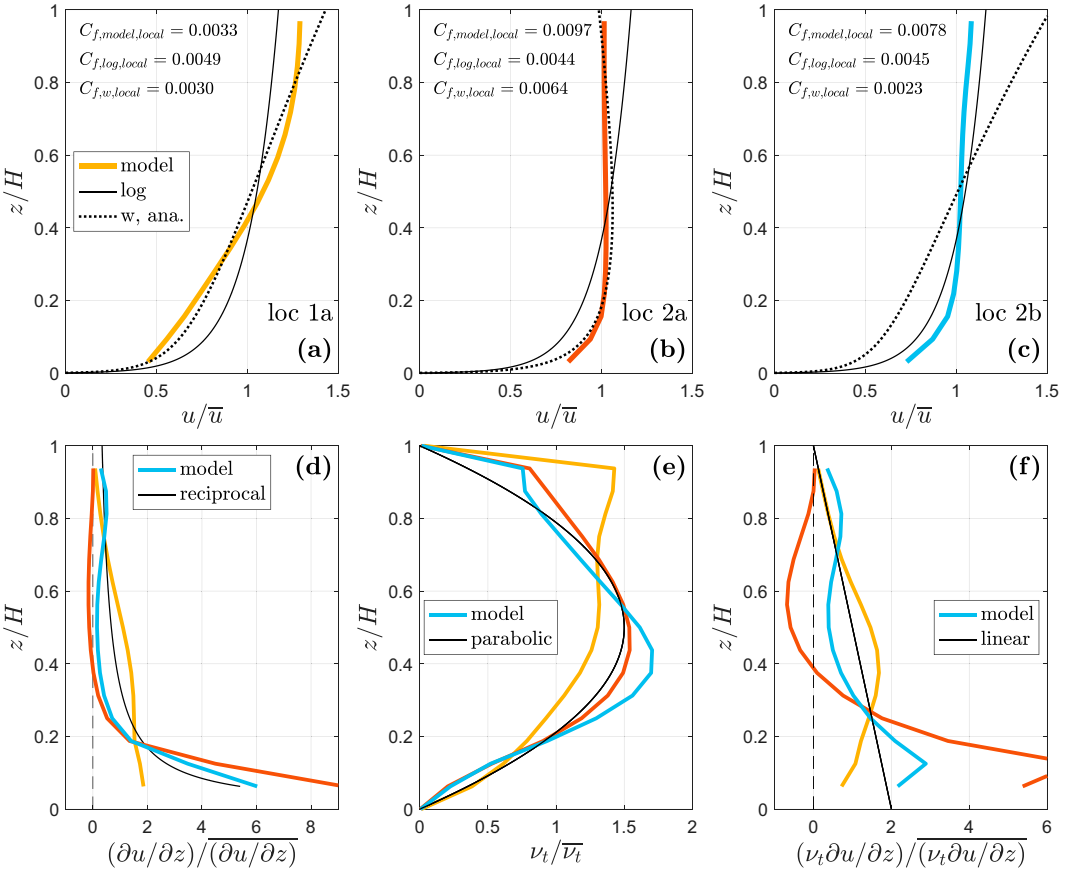

FIG. 9. The vertical profiles of flow during ebb tide. (a)–(c) Vertical profiles of streamwise velocity at three locations (marked in Fig. 8). Velocity is nondimensionalized by its depth average. Colored lines are model results. The solid black lines show the log profile, and the dotted black lines are the analytical solution with vertical advection using (23). The $C_{f,\text{model,local}}$ is the local bottom friction coefficient from the model results; $C_{f,\text{log,local}}$ is from the log assumption; $C_{f,w,\text{local}}$ is from the analytical solution with vertical advection. (d) Vertical shear. The solid black line shows a reciprocal distribution as for the log profile. (e) Eddy viscosity. The solid black line shows a parabolic distribution. (f) Shear stress. The solid black line shows a linear distribution.

using (Fig. 8b). However, the actual bottom stress shows deviations from the log-profile assumption. The actual bottom stress is enhanced compared to the log assumption, especially near the bend apex where secondary circulation is developed (Fig. 8c). This suggests that the secondary circulation alters the vertical profile of streamwise velocity and affects the bottom stress.

To investigate the momentum redistribution by secondary circulation, we examine the streamwise velocity transport equation in a cylindrical coordinate system (Batchelor 2000; Blanckaert and Graf 2004):

$$\frac{\partial u}{\partial t} = \underbrace{-\frac{1}{1+r/R}u\frac{\partial u}{\partial s}}_{\text{along-channel advection}} \underbrace{-v\frac{\partial u}{\partial r}+\frac{1}{1+r/R}\frac{uv}{R}}_{\text{lateral advection}} \underbrace{-w\frac{\partial u}{\partial z}}_{\text{vertical advection}} - \frac{1}{1+r/R}\frac{1}{\rho}\frac{\partial p}{\partial s}+\frac{\partial}{\partial z}\left(\nu_t\frac{\partial u}{\partial z}\right), \tag{18}$$

where s, r, and z represent the streamwise, lateral, and vertical coordinates, and u, v, and w are the corresponding velocity components. Here ν_t is the vertical eddy viscosity, and the horizontal viscosity is typically negligible in shallow flows. The first term on the right side represents streamwise advection; the second and third terms are the lateral advection; the fourth term is the vertical advection. The last two terms are the pressure gradient forcing (mainly due to water-level gradient) and shear stress. The last two terms are dominant in the large-scale, depth-averaged momentum balance (6), but the other advection terms can be important at the local scales investigated here.

Near the outer bank where downwelling occurs (e.g., XS1 and XS2 in Figs. 5a,b), the vertical advection tends to increase the near-bed momentum (Fig. 8d). As a result, the vertical shear is more concentrated near the bed compared to a log profile (e.g., loc 2a in Fig. 9b), and the bed shear stress is thus greater than that based on the log-profile assumption (Fig. 8c). By contrast, near the inner bank upstream of the bend apex, the upward velocity leads to decreased streamwise momentum and weaker vertical shear near the bed (e.g., loc 1a in Figs. 8c,d and 9a), and thus, the bottom friction is less than the log-profile assumption.

Near the inner bank at the bend apex (e.g., loc 2b in Figs. 8c–e and 9c), the vertical velocity is upward and tends to decrease the momentum near the bed. At the same time, the lateral velocity advects the high momentum near the bed from the outer bank toward the inner bank (XS2 in Fig. 5b). The lateral advection that tends to increase the near-bed velocity dominates over the vertical advection that acts in the opposite way, and therefore the bottom stress is enhanced. The streamwise momentum becomes homogenized in the cross sections at the bend apex and farther downstream (XS2 in Fig. 5b) as a result of the stirring (vertical and lateral advection) by secondary circulation and the bottom stress is thus enhanced across the channel (Fig. 8c).

Generally, the bottom stress deviation from the log profile has a spatial pattern through the bend that is similar to the summed momentum advection terms (Figs. 8c,f). The along-channel advection of streamwise velocity (not shown) is smaller in magnitude than the lateral and vertical advection terms and corresponds less clearly with the bottom stress enhancement.

Regions with both increased and decreased bottom stress occur in the bend due to the momentum redistribution by secondary circulation, and the integrated effect influences the overall drag at the bend scale. The bottom stress can be decreased by up to a factor of 2 compared to the classical log profile where the streamwise momentum is decreased, and can be increased by more than a factor of 2 where the near-bed vertical shear is enhanced. The overall effect of momentum redistribution by secondary circulation is to enhance the bottom stress in the bend, because more locations have increased near-bed velocity than decreased near-bed velocity and the stress has a quadratic dependence on velocity. This explains the greater calculated depth-average bottom friction coefficient $C_{f,H}$ compared to the typical log-profile prediction $C_{f,\log}$ in section 4a.

2) A 1D ANALYTICAL MODEL

The vertical advection of momentum initiates the transport of high momentum to the lower water column, and lateral advection spreads higher momentum flow near the bed across the channel. In this subsection, we develop a simplified 1D analytical model to deconstruct the complex patterns in the 3D model and conceptually frame the linkage between vertical advection and bottom shear stress enhancement.

When a steady and horizontally uniform boundary layer flow is established (without secondary flows), the streamwise momentum equation can be simplified as

$$\frac{1}{\rho}\frac{\partial p}{\partial s} = \frac{1}{\rho}\frac{\partial \tau}{\partial z} = \frac{\partial}{\partial z}\left(\nu_t \frac{\partial u}{\partial z}\right). \tag{19}$$

Equation (19) is essentially a local depth-dependent form of (6) when the large-scale form drag is not considered. $(1/\rho)\partial p/\partial s$ is vertically uniform by neglecting baroclinicity, and thus τ typically has a linear distribution in the vertical $\tau = \tau_b(1 - z/H)$. Substituting in the definition of u_* in (3), we can write

$$u_*^2\left(1 - \frac{z}{H}\right) = \nu_t \frac{\partial u}{\partial z}. \tag{20}$$

The eddy viscosity ν_t typically has a parabolic distribution in the vertical direction $\nu_t = \kappa u_* z(1 - z/H)$, and (20) thus becomes

$$u_* = \kappa z \frac{\partial u}{\partial z}. \tag{21}$$

The solution to (21) is the canonical logarithmic velocity relationship (2).

We add the vertical advection term to (20) to investigate the momentum redistribution by vertical velocity w, so

$$u_*^2\left(1 - \frac{z}{H}\right) = \nu_t \frac{\partial u}{\partial z} - wu. \tag{22}$$

On the bottom boundary w vanishes and (22) reduces to (20). Assuming a parabolic distribution for the vertical velocity $w = w_0(z/H)(1 - z/H)$, we can write

$$u_*^2 = \kappa u_* z \frac{\partial u}{\partial z} - w_0 u \frac{z}{H}. \tag{23}$$

For given z_0 and w_0, this (23) can be solved numerically to get an analytical solution to the vertical profile of u and the modification to C_f by the vertical velocity. For example, the vertical velocity is typically ~1 cm s^{-1} in the bend for ~1 m s^{-1} streamwise tidal current, and in the analytical solution, C_f is increased by 31% for a downwelling case with $w_0/\overline{u} = -0.01$ and decreased by 33% for an upwelling case with $w_0/\overline{u} = -0.01$, given $H = 5$ m and $z_0 = 0.005$ m.

Solutions to (23) are compared with model results in Fig. 9. w_0 is taken from the model results as the local normal-to-bed velocity, which squeezes or stretches the velocity profile perpendicularly relative to the boundary. Note that the normal-to-bed velocity is different from the vertical velocity in the model output because the channel bed is not flat. The analytical solutions to (23) are consistent with the velocity profiles at loc 1a and 2a, where vertical advection is dominant in the momentum transport (Fig. 8d). For these locations, the bottom friction coefficient $C_{f,w,\text{local}}$ from the analytical solution with vertical advection is consistent with the bottom stress decrease or increase, although the values of $C_{f,w,\text{local}}$ and $C_{f,\text{model,local}}$ do not match exactly. At loc 2b where lateral advection dominates over vertical advection, the 1D analytical solution fails because it does not account for the redistribution by the lateral velocity.

Generally, the analytical solution with vertical advection explains the altered bottom stress where vertical advection is dominant but it fails where lateral becomes more important. The analytical solution suggests that basic assumptions behind the log profile are not violated, e.g., the eddy viscosity ν_t is generally consistent with a parabolic distribution (Fig. 9e), but deviations of local bottom stress occur because the log-profile theory ignores the locally strong influence of vertical advection. The vertical shear $\partial u/\partial z$ is more concentrated in the lower water column where secondary circulation brings higher momentum flow toward the bed. As a result, the shear stress $\nu_t \partial u/\partial z$ is enhanced near the bed (Fig. 9f), and this contributes to the overall increase in drag with curvature.

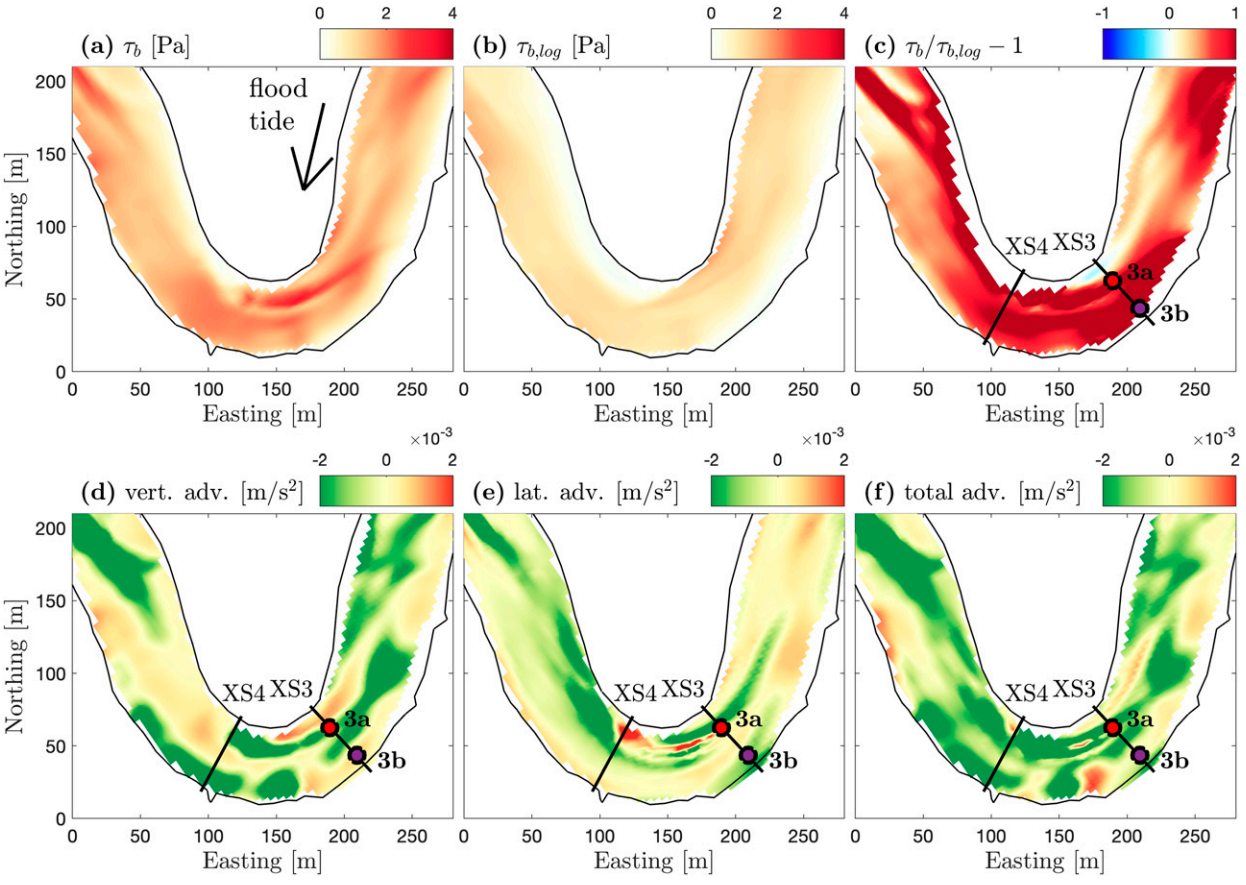

FIG. 10. As in Fig. 8, but for the flood tide bottom stress and momentum redistribution terms. (a) Bottom stress τ_b. (b) Predicted bottom stress $\tau_{b,\log}$ based on the log-profile assumption. (c) Relative difference between τ_b and $\tau_{b,\log}$. (d)–(f) The vertical, lateral, and total advection terms of along-channel velocity in (18).

3) FLOOD TIDE

During the flood tide the secondary circulation is more complex than the typical single secondary circulation cell for ebbs, but the mechanisms of momentum redistribution and bottom stress enhancement are similar. During flood tide, a surface convergence zone with strong downwelling occurs near the inner bank (Figs. 5c,d). As a result, high momentum flow is vertically injected to the lower water column and spreads laterally near the bed to enhance the bottom shear stress in the downwelling region and nearby (Fig. 10c).

Vertical advection is the dominant term for redistributing momentum in the downwelling region (e.g., loc 3a in Figs. 10d and 11a), and the analytical solution with vertical advection (23) yields velocity profiles that are consistent with the 3D model. Lateral advection is dominant adjacent to the downwelling region (e.g., loc 3b in Figs. 10e and 11b), and thus the 1D analytical solution does not explain the velocity profile. The advection by the secondary circulation concentrates the shear near the bed (Fig. 11c) and leads to locally enhanced bottom friction. In addition, a region of negative shear stress is found near the surface (Fig. 11e), because the maximum streamwise velocity occurs in the lower water column with reversed vertical shear in the upper water column. This reversal in shear is consistent with the flood tide BCPG-driven secondary circulation noted in other studies (e.g., Lacy and Monismith 2001; Lacy et al. 2003; Lerczak and Geyer 2004).

c. *Dependence on bend sharpness*

While the analysis thus far has focused on a single sharp bend (Bend-5.4), secondary circulation, flow separation, and momentum redistribution also occur in other bends of the North River estuary with different sharpness. As an example, below we highlight two other bends: Bend-4.2 has intermediate curvature with a radius of curvature $R = 140$ m, width $W = 70$ m, and curvature ratio $R/W \approx 2$, and Bend-6.7 is one of the smoothest bends in the North River with $R = 200$ m, $W = 50$ m, and $R/W \approx 4$.

1) EBB TIDE

During ebb tide, a single secondary circulation cell occurs in Bend-4.2 (Figs. 12a–d), similar to the sharper Bend-5.4. Upwelling near the inner bank tends to decrease velocity in the

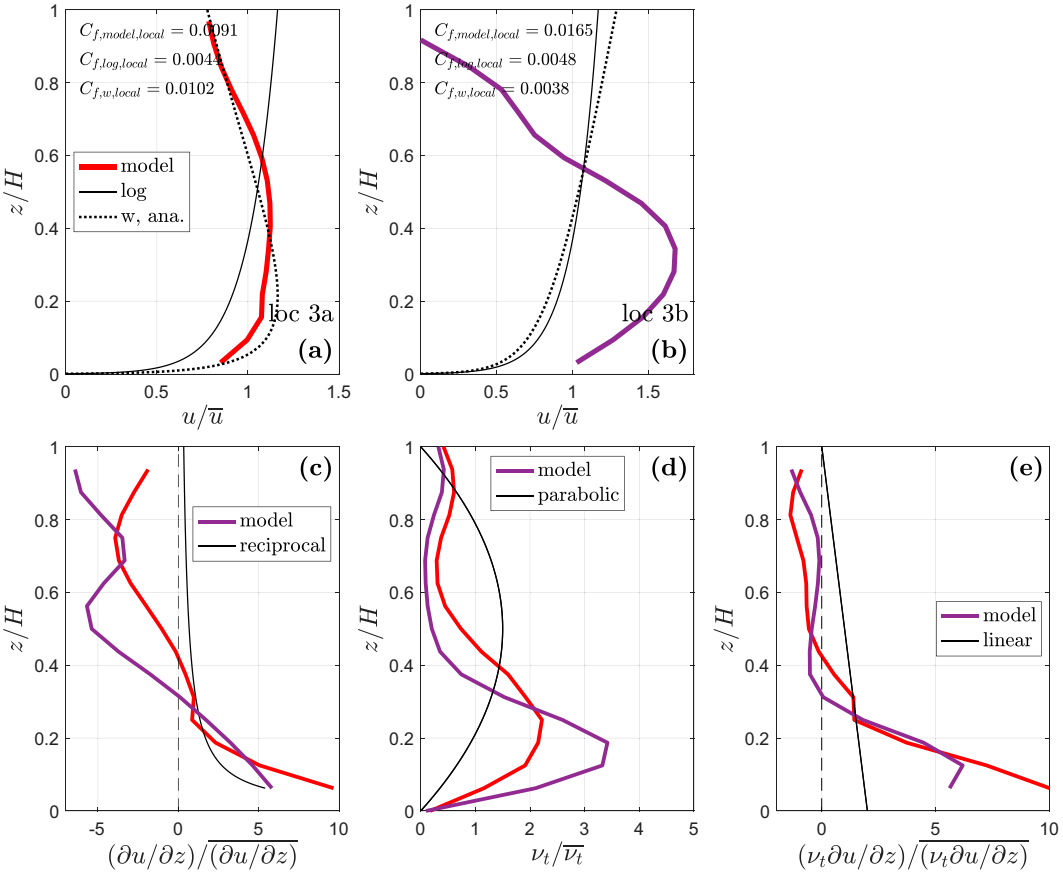

FIG. 11. As in Fig. 9, but for the vertical structures of flow during flood tide, at two locations marked in Fig. 10. (a),(b) Vertical profiles of streamwise velocity. (c) Vertical shear. (d) Eddy viscosity. (e) Shear stress.

lower water column and decrease the bed shear stress, while downwelling near the outer bank transports higher momentum flow to the low water column and increases the bed stress. Downstream of the bend apex, the higher momentum flow is advected inward by the lateral flow near the bed, leading to enhanced bottom stress across the entire cross section.

Similar helical flow is also found in the smoother Bend-6.7, leading to a region with decreased bottom stress from the inner bank of the upstream bend to the inner bank of Bend-6.7, and then shifted to the inner bank of the following bend, where upwelling decreases the near-bed velocity (Fig. 12f). Increased bottom stress is found in other regions where the near-bed momentum can be increased by secondary circulation. Although secondary circulation still affects the bottom stress in this smoothest Bend-6.7, the momentum distribution in a cross section downstream of the bend apex is more vertically sheared and less homogenized by the secondary circulation than in the sharp Bend-5.4 (Fig. 12g compared to Fig. 5b). As a result, the overall bottom friction enhancement ($C_{f,H}/C_{f,\log} - 1$) in Bend-6.7 is only around 20%. The above comparison suggests that secondary circulation is more effective at redistributing momentum and increasing bottom stress in sharp bends than in smooth bends, consistent with theories that the strength of secondary circulation increases with stronger curvature (Kalkwijk and Booij 1986; Geyer 1993; Blanckaert and De Vriend 2010; Ottevanger et al. 2012).

2) FLOOD TIDE

During flood tide, more complex secondary circulation patterns are found in both Bend-4.2 and Bend-6.7, as in the sharper Bend-5.4. Surface convergence zones with downwelling occur near the inner bank upstream of the bend apexes (Figs. 13c,g). Higher momentum flow is injected near the bed by the downward velocity and reversed vertical shear occurs near the surface. The bottom shear stress near the convergence is increased compared to the log profile and the overall bottom friction enhancement ($C_{f,H}/C_{f,\log} - 1$) is up to 50% in both Bend-4.2 and Bend-6.7.

Flow separation is found on the lee side of Bend-4.2, with a low velocity zone located near the inner bank and the main flow shifted toward the outer bank. Form drag due to the flow separation is up to 50% of the total bottom friction in Bend-4.2 (i.e., $C_{d,\mathrm{xs}}/C_{f,\mathrm{xs}}$ up to 1.5). Flow separation is less notable in the smoother Bend-6.7, which agrees with the theoretical prediction in Bo and Ralston (2020) that flow separation is less likely to occur in smooth bends. The ratio of $C_{d,\mathrm{xs}}/C_{f,\mathrm{xs}}$ is close to 1 in Bend-6.7, suggesting that the contribution from form drag is small (less than ~10%) compared to bottom friction.

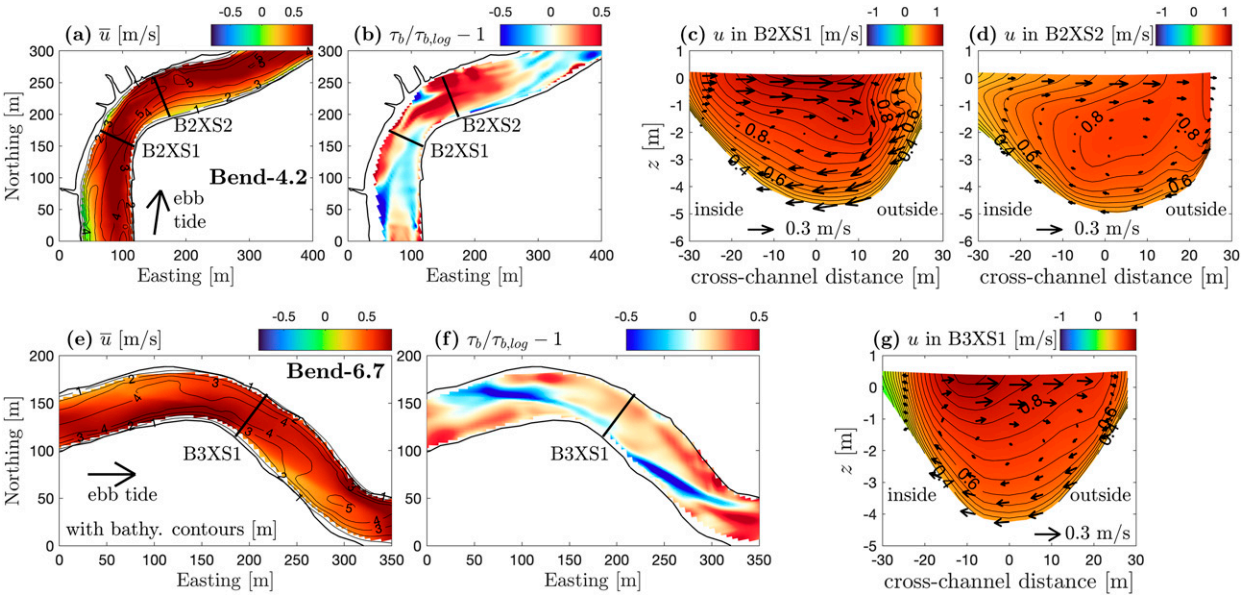

FIG. 12. Ebb tide flow field in (top) Bend-4.2 and (bottom) Bend-6.7. (a),(e) Depth-averaged along-channel velocity $\overline{u}$, with contours of bathymetry. (b),(f) Relative bottom stress alteration compared to the log-profile assumption. (c),(d),(g) Along-channel velocity u in the cross sections marked in the map views.

5. Discussion

a. *The mechanisms of drag increase in meanders*

We find that the momentum loss is increased in meanders compared with similar straight channels as a result of form drag due to flow separation, increased overall bottom stress due to the spatially variable flow field, and local enhancement of bottom stress due to momentum redistribution by the secondary circulation (Fig. 14). Flow separation creates form drag by generating a low pressure circulation zone on the lee side of the bend and results in a drag coefficient increase of nearly a factor of 2 in a sharp bend compared to the total bottom friction. Form drag is the dominant source of drag increase during flood tides when flow separation is most

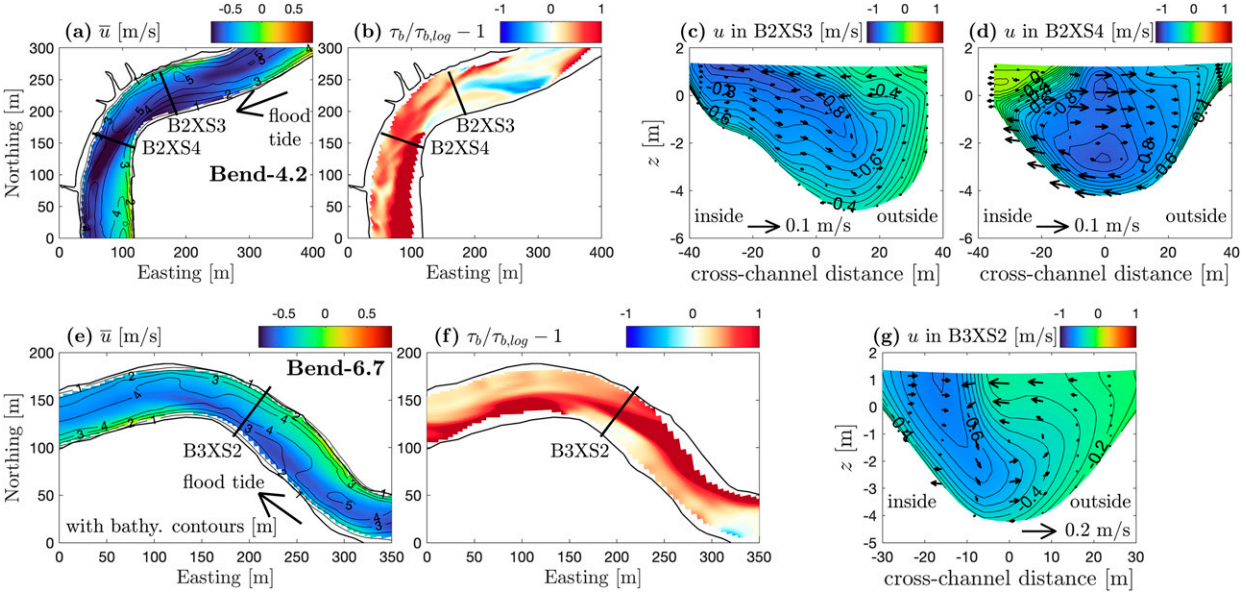

FIG. 13. As in Fig. 12, but for flood tide flow field. (a),(e) Depth-averaged along-channel velocity $\overline{u}$, with contours of bathymetry. (b),(f) Relative bottom stress alteration compared to the log-profile assumption. (c),(d),(g) Along-channel velocity u in the cross sections marked in the map views.

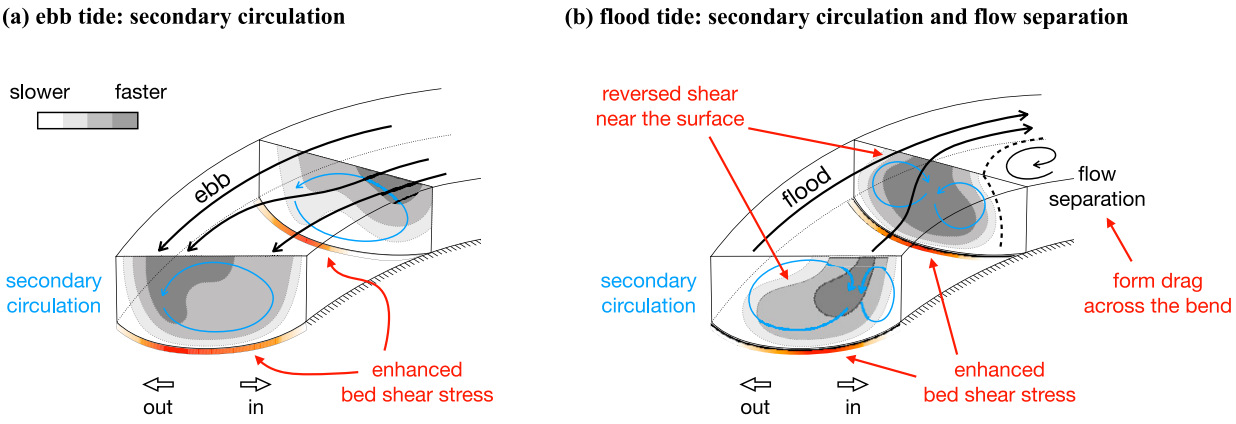

FIG. 14. Schematic plots of flow field, momentum redistribution, and drag increase in bends. (a) Ebb tide. Black arrows show the channel flow in the horizontal plane, and blue arrows show secondary circulation in cross sections. The gray colors represent streamwise momentum. Red colors show regions with enhanced bottom shear stress compared to the log-profile assumption. High momentum is advected to near the bed, which increases the bottom friction. (b) As in (a), but for flood tide. In addition to secondary circulation, flow separation creates a recirculating zone and leads to form drag across the bend.

notable, and is less important during ebb tides. The spatial variability of bathymetry and velocity and their nonlinear correlation also cause an overall increase in frictional drag for a given volume flux through the channel, although that only accounts for an increase of around 10% in the friction coefficient. Secondary circulation due to curvature advects higher momentum flow from the surface toward the lower water column in downwelling regions near the inner bank (flood tide) or outer bank (ebb tide), and the near-bottom secondary circulation spreads the high momentum laterally. As a result, the bottom shear stress is enhanced, which leads to drag increases of 30%–60% compared to the bottom stress based on assuming a classical log profile.

The drag increases due to the above mechanisms vary with bend geometry and topography. Flow separation is stronger in sharp bends (Blanckaert 2010; Bo and Ralston 2020), so form drag may be dominant in sharp bends but unimportant in smooth bends. The strength of secondary circulation also increases with channel curvature, so the momentum redistribution and bottom stress enhancement are also more significant in sharp bends (Blanckaert and De Vriend 2010; Ottevanger et al. 2012). While the drag increase due to the spatially variable flow field is not a dominant factor in the bends examined here, it may be important in bends with more complex bathymetric features.

The role of the curvature-induced secondary circulation in redistributing momentum and altering the bottom stress is not unique to this system. Similar mechanisms apply to other tidal meanders (Seim et al. 2002) and river meanders (Dietrich and Whiting 1989; Frothingham and Rhoads 2003). Moreover, secondary circulation can also affect the bottom boundary layer in systems without curvature, e.g., in straight estuarine channels with BCPG-driven secondary circulation (Nunes and Simpson 1985; Lerczak and Geyer 2004) and in large estuaries where Coriolis can dominate the secondary circulation (Valle-Levinson 2011).

The lateral component of the near-bottom velocity due to the secondary circulation can also increase the drag on the streamwise flow by creating an additional bed shear stress component (Chang 1984; Blanckaert and de Vriend 2003). However, the nonlinear advection of streamwise momentum and enhancement of streamwise bottom stress have greater contributions to the drag enhancement in this system. The lateral component of bottom stress accounts for less than 10% of the total bottom stress in the model results, because shear stress scales with velocity squared and the streamwise velocities are much greater in magnitude than the lateral velocities.

We primarily analyzed flow conditions with weak stratification, and further investigation is needed to quantify how these processes affect drag in the presence of stronger vertical or horizontal salinity gradients. Strong stratification can suppress turbulence, inhibit the vertical transport of momentum, and decrease the bottom stress (e.g., Turner and Turner 1979; Stacey and Ralston 2005; Qian et al. 2022). Moreover, strong horizontal salinity gradients can affect the momentum budget through baroclinicity and alter the secondary circulation pattern. The multiple secondary circulation cells during flood tides result from baroclinic effects (Kranenburg et al. 2019). During ebb tides, the region of interest is mostly well mixed or fresh as the salt front is advected down-estuary. As a result, baroclinicity is generally weak during ebbs and the classical helical flow occurs in the analyzed bends. In meanders where strong vertical or horizontal salinity gradients appear during ebb tides, reversed secondary circulation (Chant and Wilson 1997; Bo and Ralston 2022) or multiple layers of secondary circulation (Nidzieko et al. 2009) may occur as a result of the interaction between stratification, baroclinicity, and secondary flows. Reversed secondary circulation can influence the momentum redistribution and alter the bottom stress enhancement compared to the classical helical flow. With multiple layers of secondary circulation, the vertical advection of momentum may be inhibited compared to the classical helical flow, potentially leading to less bottom stress enhancement.

While we have focused on the momentum budget in the above analysis, the increased momentum loss due to the

channel curvature also corresponds with increased energy dissipation (Seim and Gregg 1997; Seim et al. 2006; Warner et al. 2013; Bo and Ralston 2020; Bo et al. 2021). The enhanced bottom stress associated with secondary circulation and altered velocity profiles in the vertical directly corresponds with an increased energy loss rate near the bed. Flow separation that creates form drag in the momentum budget can also contribute to the increased energy dissipation. The separation zone laterally squeezes and accelerates the main flow, which increases the spatial variability of depth-averaged velocity and increases both the overall bottom stress and the near-bed dissipation (Bo and Ralston 2020). The horizontally variable flow field can be a more important contributor to energy dissipation compared to momentum loss because of the higher-order dependence on velocity of energy than momentum. In addition to the increased energy loss near the bed, interior dissipation can occur in the bend associated with the reversed vertical shear found in the upper water column during flood tides (Figs. 5c,d and 11). This interior dissipation is not associated with the bottom boundary layer and bed friction, and could contribute to energy loss with the form drag.

b. Which C_d or C_f to choose to quantify the drag?

Our analysis shows that the drag coefficient C_d and bottom friction coefficient C_f vary depending on the choice of $\overline{u}|\overline{u}|/H$ (depth-averaged velocity squared over depth) used to scale the drag term in the depth-averaged momentum equation, especially in systems with complex bathymetry and flow distribution. For assessing the overall momentum loss in open-channel flows, the cross-sectional-average drag coefficient $C_{d,\mathrm{xs}}$ in (12) should be used because that integrates any form drag from topographic features. The $C_{d,\mathrm{xs}}$ is defined based on the along-channel average of each cross-sectional average velocity and depth $\{(\langle\overline{u}\rangle|\langle\overline{u}\rangle|)/\langle H\rangle\}$, and can be rewritten as $Q|Q|\{1/\langle H\rangle^3W^2\}$ assuming the flux $Q = \langle\overline{u}\rangle\langle H\rangle W$ is conserved along the channel. Therefore, in field observations, Q can be estimated based on the velocity and depth measurements in a single cross section, and then $\{1/\langle H\rangle^3W^2\}$ can be evaluated using an estimate of the along-channel variability of channel depth and width. Similarly, the cross-sectional-average bottom friction coefficient $C_{f,\mathrm{xs}}$ in (15) should be used to quantify the overall bottom shear stress experienced by a given amount of flux through the channel.

An alternative to quantify the bottom stress is to use the depth-average bottom friction coefficient $C_{f,H}$ in (17). In meanders, the curvature-induced flow processes can add to the spatial variability of depth-averaged velocity. In addition, complex bathymetric features that are usually found in natural channels can also affect the depth-averaged velocity distribution through topographic steering (Dietrich and Smith 1983; Blanckaert 2010; Ottevanger et al. 2012). Consequently, the difference between $C_{f,H}$ and $C_{f,\mathrm{xs}}$ may be significant. The calculation or measurement of $C_{f,H}$ can remove the drag increase due to the spatial variations in depth and depth-averaged velocity that are included in $C_{f,\mathrm{xs}}$, and thus only quantify the bottom stress associated with the vertical structure of the local flow. The $C_{f,H}$ is difficult to rigorously estimate in the field because it requires measuring velocity and depth with complete spatial coverage. Note that calculating $C_{f,H}$ based on the depth and depth-averaged velocity at a single location may introduce significant biases. The $C_{f,H}$ has to be assessed using multilocation measurements of depth and velocity that are representative of the domain. To obtain an estimate of the spatial variability of bottom stress and calculate an appropriate $C_{f,H}$, either of the following approaches may be adopted: 1) deploying moorings not only in the deep channel but also in shallow regions where large values of $\overline{u}|\overline{u}|/H$ could appear or 2) combining mooring measurements with cross-sectional surveys of the distribution of $\overline{u}|\overline{u}|/H$ under a range of tidal/flow conditions.

c. Implications for morphodynamics

The increases in drag resulting from channel curvature, particularly the mechanisms associated with bottom friction, have implications for sediment erosion and deposition and for channel meander morphodynamics. The North River estuary is ebb dominant (Kranenburg et al. 2019), so here we discuss the linkage between the ebb tide bottom stress and channel morphology in the sharp Bend-5.4. Secondary circulation tends to increase the near-bed velocity through the downward advection near the outer bank, and high momentum spreads laterally near the bed at the bend apex. The enhanced bottom stress would enhance erosion and inhibit sediment deposition in the cross section at the bend apex (Fig. 8), which can explain the observed deep scour hole and the absence of a point bar at the bend apex. By contrast, regions with decreased bottom stress due to secondary circulation upwelling extend from the inner bank of the next landward bend to the inner bank of Bend-5.4, and then to the inner bank of the next seaward bend. These regions with decreased bottom stress favor sediment deposition, and could contribute to the growth of the shallow shoals extending along-channel from the inner banks of bends.

Flow separation mainly occurs during flood tide, so its influence on channel morphology may be more limited in this ebb-dominant river. Flow separation creates a low-velocity recirculation zone that could favor sediment deposition near the inner bank on the lee side of bends (Finotello et al. 2020). Additionally, the main flow is restricted to a narrower extent of the channel cross section and thus accelerated, which may enhance sediment erosion in the center of the channel (Vermeulen et al. 2015).

6. Conclusions

We calculated the drag and friction coefficients in a sinuous estuary, and found that the momentum loss is much greater than expected for straight channels. The influence of curvature-induced processes on the momentum budget was investigated, and both flow separation and secondary circulation contribute to the drag increase in meanders. Flow separation can create form drag across a bend and is most notable during flood tides. Secondary circulation can increase the near-bed velocity through vertical and lateral advection during both ebb and flood tides, leading to increased bottom stress compared to the log-profile

assumption. The altered momentum distribution and enhanced bottom stress may affect sediment transport in the bend and contribute to the observed morphology.

Acknowledgments. The research leading to these results was funded by NSF Awards OCE-2123002 and OCE-1634481. The authors thank P. Traykovski for providing the bathymetric data and A. M. P. Garcia for helpful suggestions on model construction. Comments and suggestions provided by two anonymous reviewers are greatly appreciated.

Data availability statement. Model data supporting this study are available online at doi.org/10.5281/zenodo.7105445 and doi.org/10.5281/zenodo.7200228.

REFERENCES

Arcement, G. J., and V. R. Schneider, 1989: Guide for selecting Manning's roughness coefficients for natural channels and flood plains. USGS Water-Supply Paper 2339, 44 pp., https://pubs.usgs.gov/wsp/2339/report.pdf.

Batchelor, G. K., 2000: *An Introduction to Fluid Dynamics*. Cambridge University Press, 615 pp.

Blanckaert, K., 2010: Topographic steering, flow recirculation, velocity redistribution, and bed topography in sharp meander bends. *Water Resour. Res.*, **46**, W09506, https://doi.org/10.1029/2009WR008303.

——, 2015: Flow separation at convex banks in open channels. *J. Fluid Mech.*, **779**, 432–467, https://doi.org/10.1017/jfm.2015.397.

——, and H. J. de Vriend, 2003: Nonlinear modeling of mean flow redistribution in curved open channels. *Water Resour. Res.*, **39**, 1375, https://doi.org/10.1029/2003WR002068.

——, and W. H. Graf, 2004: Momentum transport in sharp open-channel bends. *J. Hydraul. Eng.*, **130**, 186–198, https://doi.org/10.1061/(ASCE)0733-9429(2004)130:3(186).

——, and H. De Vriend, 2010: Meander dynamics: A nonlinear model without curvature restrictions for flow in open-channel bends. *J. Geophys. Res.*, **115**, F04011, https://doi.org/10.1029/2009JF001301.

——, M. G. Kleinhans, S. J. McLelland, W. S. Uijttewaal, B. J. Murphy, A. van de Kruijs, D. R. Parsons, and Q. Chen, 2013: Flow separation at the inner (convex) and outer (concave) banks of constant-width and widening open-channel bends. *Earth Surf. Processes Landforms*, **38**, 696–716, https://doi.org/10.1002/esp.3324.

Bo, T., and D. K. Ralston, 2020: Flow separation and increased drag coefficient in estuarine channels with curvature. *J. Geophys. Res. Oceans*, **125**, e2020JC016267, https://doi.org/10.1029/2020JC016267.

——, and ——, 2022: Frontogenesis, mixing, and stratification in estuarine channels with curvature. *J. Phys. Oceanogr.*, **52**, 1333–1350, https://doi.org/10.1175/JPO-D-21-0298.1.

——, ——, W. M. Kranenburg, W. R. Geyer, and P. Traykovski, 2021: High and variable drag in a sinuous estuary with intermittent stratification. *J. Geophys. Res. Oceans*, **126**, e2021JC017327, https://doi.org/10.1029/2021JC017327.

Bricker, J. D., S. Inagaki, and S. G. Monismith, 2005: Bed drag coefficient variability under wind waves in a tidal estuary. *J. Hydraul. Eng.*, **131**, 497–508, https://doi.org/10.1061/(ASCE)0733-9429(2005)131:6(497).

Chang, H. H., 1983: Energy expenditure in curved open channels. *J. Hydraul. Eng.*, **109**, 1012–1022, https://doi.org/10.1061/(ASCE)0733-9429(1983)109:7(1012).

——, 1984: Variation of flow resistance through curved channels. *J. Hydraul. Eng.*, **110**, 1772–1782, https://doi.org/10.1061/(ASCE)0733-9429(1984)110:12(1772).

Chant, R. J., and R. E. Wilson, 1997: Secondary circulation in a highly stratified estuary. *J. Geophys. Res.*, **102**, 23 207–23 215, https://doi.org/10.1029/97JC00685.

Chow, V. T., 1959: *Open-Channel Hydraulics*. McGraw-Hill, 680 pp.

Coles, D., 1956: The law of the wake in the turbulent boundary layer. *J. Fluid Mech.*, **1**, 191–226, https://doi.org/10.1017/S0022112056000135.

Dietrich, W. E., and J. D. Smith, 1983: Influence of the point bar on flow through curved channels. *Water Resour. Res.*, **19**, 1173–1192, https://doi.org/10.1029/WR019i005p01173.

——, and P. Whiting, 1989: Boundary shear stress and sediment transport in river meanders of sand and gravel. *River Meandering*, *Water Resources Monogr.*, Vol. 12, Amer. Geophys. Union, 1–50, https://doi.org/10.1029/WM012p0001.

Einstein, H. A., and J. A. Harder, 1954: Velocity distribution and the boundary layer at channel bends. *Eos, Trans. Amer. Geophys. Union*, **35**, 114–120, https://doi.org/10.1029/TR035i001p00114.

Fagherazzi, S., E. J. Gabet, and D. J. Furbish, 2004: The effect of bidirectional flow on tidal channel planforms. *Earth Surf. Processes Landforms*, **29**, 295–309, https://doi.org/10.1002/esp.1016.

Ferguson, R. I., D. R. Parsons, S. N. Lane, and R. J. Hardy, 2003: Flow in meander bends with recirculation at the inner bank. *Water Resour. Res.*, **39**, 1322, https://doi.org/10.1029/2003WR001965.

Finotello, A., M. Ghinassi, L. Carniello, E. Belluco, M. Pivato, L. Tommasini, and A. D'Alpaos, 2020: Three-dimensional flow structures and morphodynamic evolution of microtidal meandering channels. *Water Resour. Res.*, **56**, e2020WR027822, https://doi.org/10.1029/2020WR027822.

Fong, D. A., S. G. Monismith, M. T. Stacey, and J. R. Burau, 2009: Turbulent stresses and secondary currents in a tidal-forced channel with significant curvature and asymmetric bed forms. *J. Hydraul. Eng.*, **135**, 198–208, https://doi.org/10.1061/(ASCE)0733-9429(2009)135:3(198).

Francis, H., and P. Traykovski, 2021: Development of a highly portable unmanned surface vehicle for surf zone bathymetric surveying. *J. Coastal Res.*, **37**, 933–945, https://doi.org/10.2112/JCOASTRES-D-20-00143.1.

Friedrichs, C. T., and L. D. Wright, 1997: Sensitivity of bottom stress and bottom roughness estimates to density stratification, Eckernförde Bay, southern Baltic Sea. *J. Geophys. Res.*, **102**, 5721–5732, https://doi.org/10.1029/96JC03550.

Frothingham, K. M., and B. L. Rhoads, 2003: Three-dimensional flow structure and channel change in an asymmetrical compound meander loop, Embarras River, Illinois. *Earth Surf. Processes Landforms*, **28**, 625–644, https://doi.org/10.1002/esp.471.

Garcia, A. M. P., W. R. Geyer, and N. Randall, 2022: Exchange flows in tributary creeks enhance dispersion by tidal trapping. *Estuaries Coasts*, **45**, 363–381, https://doi.org/10.1007/s12237-021-00969-4.

Geyer, W. R., 1993: Three-dimensional tidal flow around headlands. *J. Geophys. Res.*, **98**, 955–966, https://doi.org/10.1029/92JC02270.

——, J. H. Trowbridge, and M. M. Bowen, 2000: The dynamics of a partially mixed estuary. *J. Phys. Oceanogr.*, **30**, 2035–2048, https://doi.org/10.1175/1520-0485(2000)030<2035:TDOAPM>2.0.CO;2.

Gross, E. S., J. R. Koseff, and S. G. Monismith, 1999: Three-dimensional salinity simulations of south San Francisco Bay. *J. Hydraul. Eng.*, **125**, 1199–1209, https://doi.org/10.1061/(ASCE)0733-9429(1999)125:11(1199).

Haidvogel, D. B., and Coauthors, 2008: Ocean forecasting in terrain-following coordinates: Formulation and skill assessment of the regional ocean modeling system. *J. Comput. Phys.*, **227**, 3595–3624, https://doi.org/10.1016/j.jcp.2007.06.016.

Johnson, G. C., and D. R. Ohlsen, 1994: Frictionally modified rotating hydraulic channel exchange and ocean outflows. *J. Phys. Oceanogr.*, **24**, 66–78, https://doi.org/10.1175/1520-0485(1994)024<0066:FMRHCE>2.0.CO;2.

Kalkwijk, J. P. T., and R. Booij, 1986: Adaptation of secondary flow in nearly-horizontal flow. *J. Hydraul. Res.*, **24**, 19–37, https://doi.org/10.1080/00221688609499330.

Kimball, P., and Coauthors, 2014: The WHOI Jetyak: An autonomous surface vehicle for oceanographic research in shallow or dangerous waters. *2014 IEEE/OES Autonomous Underwater Vehicles (AUV)*, Oxford, MS, Institute of Electrical and Electronics Engineers, 1–7, https://doi.org/10.1109/AUV.2014.7054430.

Kranenburg, W. M., W. R. Geyer, A. M. P. Garcia, and D. K. Ralston, 2019: Reversed lateral circulation in a sharp estuarine bend with weak stratification. *J. Phys. Oceanogr.*, **49**, 1619–1637, https://doi.org/10.1175/JPO-D-18-0175.1.

Lacy, J. R., and S. G. Monismith, 2001: Secondary currents in a curved, stratified, estuarine channel. *J. Geophys. Res.*, **106**, 31 283–31 302, https://doi.org/10.1029/2000JC000606.

——, M. T. Stacey, J. R. Burau, and S. G. Monismith, 2003: Interaction of lateral baroclinic forcing and turbulence in an estuary. *J. Geophys. Res.*, **108**, 3089, https://doi.org/10.1029/2002JC001392.

Langbein, W. B., and L. B. Leopold, 1970: River meanders and the theory of minimum variance. *Rivers and River Terraces*, G. H. Dury, Ed., Springer, 238–263.

Leeder, M. R., and P. H. Bridges, 1975: Flow separation in meander bends. *Nature*, **253**, 338–339, https://doi.org/10.1038/253338a0.

Lentz, S. J., K. A. Davis, J. H. Churchill, and T. M. DeCarlo, 2017: Coral reef drag coefficients–water depth dependence. *J. Phys. Oceanogr.*, **47**, 1061–1075, https://doi.org/10.1175/JPO-D-16-0248.1.

Leopold, L. B., and M. G. Wolman, 1960: River meanders. *Geol. Soc. Amer. Bull.*, **71**, 769–793, https://doi.org/10.1130/0016-7606(1960)71[769:RM]2.0.CO;2.

——, R. A. Bagnold, M. G. Wolman, and L. M. Brush, 1960: Flow resistance in sinuous or irregular channels. USGS Professional Paper 282-D, 33 pp., https://pubs.usgs.gov/pp/0282d/report.pdf.

Lerczak, J. A., and W. R. Geyer, 2004: Modeling the lateral circulation in straight, stratified estuaries. *J. Phys. Oceanogr.*, **34**, 1410–1428, https://doi.org/10.1175/1520-0485(2004)034<1410:MTLCIS>2.0.CO;2.

Marani, M., S. Lanzoni, D. Zandolin, G. Seminara, and A. Rinaldo, 2002: Tidal meanders. *Water Resour. Res.*, **38**, 1225, https://doi.org/10.1029/2001WR000404.

McCabe, R. M., P. MacCready, and G. Pawlak, 2006: Form drag due to flow separation at a headland. *J. Phys. Oceanogr.*, **36**, 2136–2152, https://doi.org/10.1175/JPO2966.1.

Monin, A. S., and A. M. Yaglom, 1971: *Statistical Fluid Mechanics*: *Mechanics of Turbulence*. Vol. 1, Dover, 784 pp.

Mukai, A. Y., J. J. Westerink, R. A. Luettich Jr., and D. Mark, 2002: Eastcoast 2001, a tidal constituent database for western North Atlantic, Gulf of Mexico, and Caribbean Sea. Tech. Rep. ERDC/CHL TR-02-24, 196 pp., https://apps.dtic.mil/sti/pdfs/ADA408733.pdf.

Murphy, A. H., 1988: Skill scores based on the mean square error and their relationships to the correlation coefficient. *Mon. Wea. Rev.*, **116**, 2417–2424, https://doi.org/10.1175/1520-0493(1988)116<2417:SSBOTM>2.0.CO;2.

Nanson, R. A., 2010: Flow fields in tightly curving meander bends of low width-depth ratio. *Earth Surf. Processes Landforms*, **35**, 119–135, https://doi.org/10.1002/esp.1878.

Nepf, H., 1999: Drag, turbulence, and diffusion in flow through emergent vegetation. *Water Resour. Res.*, **35**, 479–489, https://doi.org/10.1029/1998WR900069.

Nidzieko, N. J., J. L. Hench, and S. G. Monismith, 2009: Lateral circulation in well-mixed and stratified estuarine flows with curvature. *J. Phys. Oceanogr.*, **39**, 831–851, https://doi.org/10.1175/2008JPO4017.1.

Nunes, R. A., and J. H. Simpson, 1985: Axial convergence in a well-mixed estuary. *Estuarine Coastal Shelf Sci.*, **20**, 637–649, https://doi.org/10.1016/0272-7714(85)90112-X.

Ortals, C., O. Cordero, A. Valle-Levinson, and C. Angelini, 2021: Flows, transport, and effective drag in intertidal salt marsh creeks. *J. Geophys. Res. Oceans*, **126**, e2021JC017357, https://doi.org/10.1029/2021JC017357.

Ott, M. W., and C. Garrett, 1998: Frictional estuarine flow in Juan de Fuca Strait, with implications for secondary circulation. *J. Geophys. Res.*, **103**, 156 57–15 666, https://doi.org/10.1029/98JC00019.

Ottevanger, W., K. Blanckaert, and W. S. J. Uijttewaal, 2012: Processes governing the flow redistribution in sharp river bends. *Geomorphology*, **163–164**, 45–55, https://doi.org/10.1016/j.geomorph.2011.04.049.

Qian, S., J. Zhang, D. Wang, and Y. P. Wang, 2022: Observational study on drag reduction of continental-shelf bottom boundary layer. *Phys. Fluids*, **34**, 055127, https://doi.org/10.1063/5.0091335.

Ralston, D. K., G. W. Cowles, W. R. Geyer, and R. C. Holleman, 2017: Turbulent and numerical mixing in a salt wedge estuary: Dependence on grid resolution, bottom roughness, and turbulence closure. *J. Geophys. Res. Oceans*, **122**, 692–712, https://doi.org/10.1002/2016JC011738.

Rogers, J. S., S. A. Maticka, V. Chirayath, C. B. Woodson, J. J. Alonso, and S. G. Monismith, 2018: Connecting flow over complex terrain to hydrodynamic roughness on a coral reef. *J. Phys. Oceanogr.*, **48**, 1567–1587, https://doi.org/10.1175/JPO-D-18-0013.1.

Schnauder, I., and A. N. Sukhodolov, 2012: Flow in a tightly curving meander bend: Effects of seasonal changes in aquatic macrophyte cover. *Earth Surf. Processes Landforms*, **37**, 1142–1157, https://doi.org/10.1002/esp.3234.

Seim, H., J. Blanton, and S. Elston, 2006: Tidal circulation and energy dissipation in a shallow, sinuous estuary. *Ocean Dyn.*, **56**, 360–375, https://doi.org/10.1007/s10236-006-0078-x.

Seim, H. E., and M. C. Gregg, 1997: The importance of aspiration and channel curvature in producing strong vertical mixing over a sill. *J. Geophys. Res.*, **102**, 3451–3472, https://doi.org/10.1029/96JC03415.

——, J. O. Blanton, and T. Gross, 2002: Direct stress measurements in a shallow, sinuous estuary. *Cont. Shelf Res.*, **22**, 1565–1578, https://doi.org/10.1016/S0278-4343(02)00029-8.

Shchepetkin, A. F., and J. C. McWilliams, 2005: The Regional Oceanic Modeling System (ROMS): A split-explicit, free-surface, topography-following-coordinate oceanic model. *Ocean Modell.*, **9**, 347–404, https://doi.org/10.1016/j.ocemod.2004.08.002.

Signell, R. P., and W. R. Geyer, 1991: Transient eddy formation around headlands. *J. Geophys. Res.*, **96**, 2561–2575, https://doi.org/10.1029/90JC02029.

Soulsby, R., 1990: Tidal-current boundary layers. *Ocean Engineering Science*, B. L. Méhauté and D. M. Hanes, Eds., *The Sea—Ideas and Observations on Progress in the Study of the Seas*, Vol. 9, John Wiley and Sons, 523–566.

Stacey, M. T., and D. K. Ralston, 2005: The scaling and structure of the estuarine bottom boundary layer. *J. Phys. Oceanogr.*, **35**, 55–71, https://doi.org/10.1175/JPO-2672.1.

Thomson, J., 1877: V. On the origin of windings of rivers in alluvial plains, with remarks on the flow of water round bends in pipes. *Proc. Roy. Soc. London*, **25**, 5–8, https://doi.org/10.1098/rspl.1876.0004.

Trowbridge, J. H., and S. J. Lentz, 2018: The bottom boundary layer. *Annu. Rev. Mar. Sci.*, **10**, 397–420, https://doi.org/10.1146/annurev-marine-121916-063351.

Turner, J. S., and J. S. Turner, 1979: *Buoyancy Effects in Fluids*. Cambridge University Press, 367 pp.

Umlauf, L., and H. Burchard, 2003: A generic length-scale equation for geophysical turbulence models. *J. Mar. Res.*, **61**, 235–265, https://doi.org/10.1357/002224003322005087.

Valle-Levinson, A., 2011: Large estuaries (effects of rotation). *Treatise on Estuarine and Coastal Science*, Vol. 2, E. Wolanski and D. McLusky, Eds., Academic Press, 123–139, https://doi.org/10.1016/B978-0-12-374711-2.00208-4.

Vermeulen, B., A. Hoitink, and R. J. Labeur, 2015: Flow structure caused by a local cross-sectional area increase and curvature in a sharp river bend. *J. Geophys. Res. Earth Surf.*, **120**, 1771–1783, https://doi.org/10.1002/2014JF003334.

Warner, J. C., C. R. Sherwood, H. G. Arango, and R. P. Signell, 2005: Performance of four turbulence closure models implemented using a generic length scale method. *Ocean Modell.*, **8**, 81–113, https://doi.org/10.1016/j.ocemod.2003.12.003.

——, ——, R. P. Signell, C. K. Harris, and H. G. Arango, 2008: Development of a three-dimensional, regional, coupled wave, current, and sediment-transport model. *Comput. Geosci.*, **34**, 1284–1306, https://doi.org/10.1016/j.cageo.2008.02.012.

——, B. Armstrong, R. He, and J. B. Zambon, 2010: Development of a Coupled Ocean–Atmosphere–Wave–Sediment Transport (COAWST) modeling system. *Ocean Modell.*, **35**, 230–244, https://doi.org/10.1016/j.ocemod.2010.07.010.

Warner, S. J., P. MacCready, J. N. Moum, and J. D. Nash, 2013: Measurement of tidal form drag using seafloor pressure sensors. *J. Phys. Oceanogr.*, **43**, 1150–1172, https://doi.org/10.1175/JPO-D-12-0163.1.